Article

Biosynthesis; Characterization; and Antibacterial, Antioxidant, and Docking Potentials of Doped Silver Nanoparticles Synthesized from Pine Needle Leaf Extract

Nourhane A. Darwich [1],*, Malak Mezher [1], Alaa M. Abdallah [2], Ahmed F. El-Sayed [3,4], Rana El Hajj [1], Taymour A. Hamdalla [5] and Mahmoud I. Khalil [1,6],*

1   Department of Biological Sciences, Faculty of Science, Beirut Arab University, Beirut P.O. Box 11-5020, Lebanon; mezher.malak@outlook.com (M.M.); r.hajj@bau.edu.lb (R.E.H.)
2   Department of Physics, Faculty of Science, Beirut Arab University, Beirut P.O. Box 11-5020, Lebanon; a.mabdallah@bau.edu.lb
3   Microbial Genetics Department, Biotechnology Research Institute, National Research Centre, Giza 12622, Egypt; ahmedfikry.nrc@gmail.com
4   Egypt Center for Research and Regenerative Medicine (ECRRM), Cairo 11517, Egypt
5   Physics Department, Faculty of Science, University of Tabuk, Tabuk 47512, Saudi Arabia; t-ahmed@ut.edu.sa
6   Molecular Biology Unit, Department of Zoology, Faculty of Science, Alexandria University, Alexandria 21568, Egypt
*   Correspondence: nourhandarwish7@gmail.com (N.A.D.); m.khalil@bau.edu.lb or mahmoud_ibrahim@alexu.edu.eg (M.I.K.)

Abstract: The current study focused on the synthesis of doped silver nanoparticles (doped AgNPs) with yttrium (Y), gadolinium (Gd), and chromium (Cr) from pine needle leaf extract (PNLE). X-ray diffraction (XRD) was performed to assess the phase formation, detecting 61.83% from Ag and 38.17% for secondary phases of AgCl, AgO, Y, Cr-, and Gd phases. The size and shape of the NPs were determined by transmission electron microscopy (TEM), showing a spherical shape with an average particle size of 26.43 nm. X-ray photoelectron spectroscopy (XPS) detected the oxidation state of the presented elements. The scanning electron microscope (SEM) and the energy-dispersive X-ray analysis (EDX) determined the morphology and elemental composition of the NPs, respectively. Fourier transform infrared spectroscopy (FTIR) determined the different functional groups indicating the presence of Ag, Y, Gd, Cr, and other groups. Photoluminescence (PL) spectroscopy showed the optical properties of the NPs. A vibrating sample magnetometer (VSM) revealed the ferromagnetic behavior of the doped AgNPs. The antibacterial activity of the doped AgNPs was tested against six uro-pathogenic bacteria (*Staphylococcus aureus*, *Staphylococcus haemolyticus*, *Enterococcus faecalis*, *Escherichia coli*, *Klebsiella pneumonia*, and *Pseudomonas aeruginosa*) using the minimum inhibitory concentration (MIC) and minimum bactericidal concentration (MBC) microdilution assays, agar well diffusion assay, time–kill test, and antibiofilm screening assays, revealing significant activity, with MICs ranging between 0.0625 and 0.5 mg/mL and antibiofilm activity between 40 and 85%. The antioxidant activity was determined by the 1,1, diphenyl 1-2 picrylhydrazyl (DPPH) radical scavenging assay with a potential of 61.3%. The docking studies showed that the doped AgNPs had the potential to predict the inhibition of crucial enzymes such as penicillin-binding proteins, LasR-binding proteins, carbapenemase, DNA gyrase, and dihydropteroate synthase. The results suggest that the doped AgNPs can be applied in different medical domains.

Keywords: silver nanoparticles; doping; characterization; antibacterial; antioxidant; antibiofilm; docking

1. Introduction

Antimicrobial resistance is now considered one of the biggest threats to global health, with increasing awareness of this over the recent years [1,2]. The extensive use of antibiotics

has increased the risk of developing drug-resistant bacteria [3]. It is estimated that within the next three decades, drug-resistant microbes will cause 2.4 million deaths worldwide, costing $3.5 billion a year. Furthermore, predictions suggest that by 2050, deaths from antibiotic-resistant infections will become the leading cause of mortality worldwide [4]. These facts highlight an urgent need for more targeted and effective treatments against this escalation in antibiotic resistance.

Nanotechnology has emerged as a significant strategy for finding alternatives for treating bacterial infections. Over the last few decades, it has shown promise in various fields, including biomedical sciences, nano-electronics, and consumer products [5]. Among the different nanomaterials, metallic nanoparticles (NPs) are notable due to their unique properties, such as their high surface-to-volume ratio and small size, which enhance mobility and targeted drug delivery capability [6,7]. Among others, silver NPs (AgNPs) are highly efficient, with a wide application range and broad-spectrum microbial bioactivity [8–10]. Interestingly, doping NPs allow for adjustment while maintaining a large surface area, thus improving their performance. Doping in cationic sites can significantly improve the materials' electrical, optical, magnetic, and chemical properties.

The global drive for eco-friendly NP production has led to the development of new technologies and the exploration of different synthesis resources. Stabilizing methods yielding stable, eco-friendly NPs are in high demand. This explains the high popularity of green synthesis as it enables a "biological corona" formation around NPs, which stabilizes them [11]. During synthesis, the corona layer forms around NPs. This is usually due to the biological components of the synthesis medium. Corona does not only stabilize NPs but also significantly impacts their properties and activities. This includes antibacterial efficacy, catalytic performance, and cellular interactions. The composition and structure of the corona are intimately tied to its proximate biological environment, which gives rise to dynamic context-dependent effects on NP behavior. Optimizing their performance for different uses and tailoring NP characteristics require proper comprehension of the role played by biological corona [12,13].

This involves reducing metal salts using biomaterials and stabilizing the resulting NPs, enhancing their biocompatibility and functional behavior [13]. The easiest route is employing biological resources like microorganisms or plants since they can produce uniform and stable NPs extracellularly or intracellularly [12,13]. However, there are challenges associated with microbial methods, such as specific growth conditions, energy-intensive incubation, and complex purification processes involving centrifugation, washing, and, sometimes, ultrasonication to collect intracellular NPs [14]. On the other hand, utilizing plants could overcome green synthesis challenges since various species show efficiency in rapidly producing simple yet eco-friendly NPs without requiring much energy [15]. Green synthesis challenges can be overcome by utilizing plants. Various plant species efficiently produce simple and eco-friendly NPs quickly, without energy-heavy methods [15]. Typically, plant-derived nanomaterials are produced within seconds to minutes, and stability, biocompatibility, and uniformity, among other factors, are some of their distinguishing features [15]. Medicinal plants are desirable due to their ability to enhance corona through extracts, thus making them more effective for specific applications [12,14].

Nanotechnology finds application in the biomedical and material sciences, with a wide range of uses, including drug delivery and cancer therapy. One particularly promising strategy is doping metal oxide NPs with dopants such as gadolinium (Gd), yttrium (Y), and chromium (Cr), thus enhancing their properties for further applications in biomedical and environmental fields [16]. For instance, Y enhances antioxidant activity [17]. Gd enhances NPs' magnetic properties, making them suitable for magnetic resonance imaging (MRI) [18]. On the other hand, the incorporation of Cr enhances the optical and electronic functionalities of NPs, consequently enhancing their photocatalytic performance for environmental needs, usefulness for cancer treatment, and activity as antioxidants [19]. Doped nanoparticles are stable and can, therefore, be employed in many biomedical and environmental fields. Gyawali et al. (2024) concentrated on synthetic silver nanoparticles doped

with chromium, incorporating silver nanoparticles with renowned enhanced antibacterial and catalytic activity. It was established that chromium doping increased membrane and ROS production, thus enhancing antibacterial activity against both Gram-positive and Gram-negative bacteria [20].

Y, Gd, and Cr are transition metals and rare-earth elements that hold great promise in biological applications. Their unique chemical and physical characteristics contribute to synthesized nanomaterials improved biological performance, instilling optimism and hope for future applications. Yttrium plays a significant role as an antibacterial and antioxidant agent [17]. Its antibacterial applications are diverse, with yttrium compounds and NPs damaging cell walls, impeding cell division and growth, and causing intracellular oxidative damage, ultimately leading to bacterial death. Additionally, its catalytic activities promote specific biologically-mediated processes such as oxidative reactions. As an antioxidant, yttrium neutralizes free radicals, reduces oxidation stress, and protects cells from damage, thus enhancing cellular health and highlighting its potential in biomedical applications [21]. Gadolinium is particularly important as an antibacterial agent. Gadolinium NPs can disrupt bacterial cell membranes and generate reactive oxygen species (ROS), leading to oxidative stress and cell death. Furthermore, gadolinium ions can interfere with essential enzymes that are involved in inhibiting bacterial growth [22]. Chromium NPs also possess significant antimicrobial activity. This activity can enhance nanomaterials' antibacterial efficacy, among other therapeutic uses [19].

To the best of our knowledge, this is the first study to describe the biosynthesis of yttrium (Y)-, gadolinium (Gd)-, and chromium (Cr)-doped AgNPs using pine needle leaf extract (PNLE). In this study, we aimed to synthesize doped AgNPs using PNLE. The synthesized NPs were characterized through various methods, including X-ray diffraction (XRD), transmission electron microscopy (TEM), X-ray photoelectron spectroscopy (XPS), scanning electron microscopy (SEM), Fourier transfer infrared spectroscopy (FTIR), UV–visible spectrometry (UV-vis), photoluminescence (PL) spectroscopy, and a vibrating sample magnetometer (VSM) to evaluate their physicochemical properties. We also assessed their antibacterial, antibiofilm, antioxidant, and docking capacities against Gram-positive and Gram-negative bacteria.

2. Materials and Methods

2.1. Pine Needle Collection and Extract Preparation

Green pine needles were collected from *Pinus pinea* trees from the Aishiya pine forest in Jezzine, South Lebanon. The needles were thoroughly washed several times with distilled water to wash off the dust, rinsed until no water droplets were left on the surface, and dried. Then, the needles were dried and cut into small portions. Next, 6 g of the needles were used for extraction and added to 300 mL of distilled water. The mixture was heated to 60 °C with stirring at 120 rpm for 30 min. Finally, the prepared pine needle aqueous extract was filtered under a vacuum until its temperature was lowered to room temperature, and the sample was directly used to synthesize the NPs.

2.2. Biosynthesis of the Doped AgNPs

The doped AgNPs were synthesized using a biogenic method involving the PNLE. Initially, 0.042 g of $AgNO_3$ along with 0.09 g of yttrium nitrate (YNO_3), 0.11 g of gadolinium nitrate ($GdNO_3$), and 0.1 g of chromium nitrate ($CrNO_3$) were added separately to 250 mL of the PNLE and heated at 60 °C for 30 min. The biosynthesis of the doped AgNPs began initially with the separate preparation of each NP type alone: silver (AgNPs), yttrium (YNPs), gadolinium (GdNPs), and chromium (CrNPs), all synthesized using the PNLE. After synthesis, each synthesized NP was centrifuged to separate the supernatant, and the pellet of each NP was retained. The resulting pellets were re-suspended in 15 mL of distilled water. The NP suspensions (AgNPs, YNPs, GdNPs, and CrNPs) were combined into one beaker in equal volumes (15 mL each). The mixture, in a total volume of 60 mL, was continuously stirred for 90 min. A color change from yellowish to dark

brown indicated the reduction and formation of the NPs. This mixture was centrifuged at 10,000 rpm for 10 min. After carefully removing the supernatant, the pellet was collected and placed in an oven at 60 °C for 24 h to dry and form a powder, which was then weighed.

2.3. Characterization Techniques

2.3.1. X-Ray Diffraction (XRD)

XRD profiles of the doped AgNPs were recorded by a Bruker D8 Advance system using Cu-K$_\alpha$ radiation (λ = 1.54060 Å) with a 2θ scan speed of 0.02°/s in a step of 0.1°, ranging between 20 and 80° 2θ. Then, the acquired XRD patterns were fitted with the Rietveld method employed in MAUD software version 2.992. The refinement processes identified the phases by inspecting the XRD patterns and comparing the data with the corresponding CIF files downloaded using the Crystallography Open Database (COD).

2.3.2. Transmission Electron Microscopy (TEM)

The surface morphology and particle size distribution of the doped AgNPs were investigated using a transmission electron microscope (TEM, JEOL JEM-100 CX microscope, OH, USA) operating at 80 kV with a resolution of 0.1 nm. TEM images were captured at a magnification of 100 nm and subsequently utilized for the particle size distribution measurements through ImageJ software (version 1.54g).

2.3.3. X-Ray Photoelectron Spectroscopy (XPS)

The elemental composition and oxidation state of the doped AgNPs were investigated using X-ray photoelectron spectroscopy (XPS). These measurements were carried out using a K-alpha instrument from Thermo Fisher Scientific, OH, USA, Central Metallurgical Research & Development Institute, Helwan, Egypt, with a micro-focused Al-K$_\alpha$ X-ray source. XPS experiments were performed under pressures of 10^{-9} mbar, using a pass energy of 200 eV for the full-scan spectrum and 50 eV for high-resolution HR-XPS.

2.3.4. Scanning Electron Microscopy (SEM) and Energy-Dispersive X-Ray (EDX)

The elemental composition of the prepared samples was confirmed by SEM and EDX measurements that were carried out employing a JEOL JCM-6000PLUS coupled with an EX-54450U1S61 detector, OH, USA on various regions of the samples at 10 keV.

2.3.5. Fourier Transform Infrared Spectroscopy (FTIR)

The functional groups of the samples were analyzed using a Nicolet iS5 FTIR-8400S spectrophotometer (Thermo Fisher Scientific, USA). The experiments were conducted at room temperature in the 4000–400 cm^{-1} spectral range. The samples for FTIR measurements were prepared using 2 mg of each sample integrated with a 1:100 mixture of potassium bromide (KBr), and the resulting mixture was pressed at 13,790 kPa to produce disc-shaped samples.

2.3.6. UV–Visible Spectroscopy (UV–Vis)

A UV–vis spectrophotometer (V-670; Jasco, Tokyo, Japan) was used to evaluate the optical properties of the samples at room temperature, covering the wavelength between 200 and 700 nm. After washing the NP samples, the supernatant was discarded. Samples were evaporated over the addition of distilled water until a noticeable color change indicating a stock solution was observed. Then, 400 μL of this solution was added to cuvettes, and distilled water was brought to the required volume and used as a blank solution.

2.3.7. Photoluminescence (PL)

A photoluminescence (PL) spectrum was acquired using a JASCO-FP-8600 fluorescence spectrometer (Jasco, Japan) with a Xenon (Xe) laser. For this analysis, the same sample as in the UV–visible measurements was employed, using an excitation wavelength of 420 nm.

2.3.8. Vibrating Sample Magnetometry (VSM)

The magnetic characteristics of the samples were investigated at room temperature using a Lakeshore 7410 VSM (Lakeshore Cryotronics, OH, USA). The magnetic field applied ranged from -20 to $+20$ kG.

2.4. Antibacterial Activity of the Doped AgNPs

2.4.1. Preparation of Bacterial Suspensions

The bacteria were clinically isolated from urine samples. After isolation, the suspensions were prepared by inoculating a colony from an overnight cultivated culture on nutrient agar (NA) into nutrient broth (NB) and adjusting the turbidity to 0.5 McFarland [23].

2.4.2. Broth Microdilution Assay for Detecting the Minimum Inhibitory Concentrations (MICs) and Minimum Bactericidal Concentrations (MBCs) of the Doped AgNPs

The doped AgNPs were diluted using autoclaved distilled water to obtain solutions of concentrations ranging between 0.0625 and 1 mg/mL. After adding 90 μL of NB and 10 μL of the bacterial suspensions, 100 μL of the prepared doped AgNPs and doxycycline (Dox; reference antibiotic) were added to the wells. The plates were incubated at 37 °C for 24 h, and the optical density (O.D.) was measured at 595 nm using an ELISA microtiter plate reader. The MICs were established as the lowest NP concentrations that prevented the visible growth of bacteria. The MBCs were determined by adding 10 μL of the clear wells on the Muller Hinton agar (MHA) and placing them in an incubator at 37 °C for 24 h. The MBCs were described as the lowest concentrations that did not allow the growth of bacteria [23]. All experiments were repeated at least three times.

2.4.3. Agar Well Diffusion for Detecting the Zones of Inhibition (ZOIs) of the Doped AgNPs

The test was conducted by distributing 100 μL of the prepared bacterial suspensions on MHA plates. Five minutes later, wells were created by punching the agar with a sterile cork borer of 6 mm in diameter. Then, 100 μL of the prepared solutions of the doped AgNPs, with concentrations ranging between 0.0625 and 1 mg/mL, were introduced to the wells. Dox was used as a reference antibiotic. The ZOI diameters were determined at 37 °C after 24 h of incubation [23]. The experiments were carried out in triplicate.

2.4.4. Time–Kill Test for Detecting the Time Needed by the Doped AgNPs to Inhibit Bacterial Growth

The test included the addition of 90 μL NB and 10 μL of the previously prepared bacterial suspensions, followed by adding 100 μL of the MICs of the doped AgNPs into 96-well microplates and incubating them at 37 °C for different intervals of time. The times were determined by measuring the O.D. of bacterial growth at 595 nm within the time interval (0–24 h) [24–27]. The experiment was repeated at least three times.

2.4.5. Anti-Biofilm Assay for the Detection of the Ability of the Doped AgNPs to Inhibit the Formation of Biofilms and Eradicate Pre-Formed Biofilms

The test was performed by incubating 10 μL of the prepared bacterial suspensions with 90 μL of NB in 96-well microplates. The plates were incubated at 37 °C for 3 h to attach the cells of the biofilms. Then, 100 μL of the prepared doped AgNPs at concentrations ranging between 0.0625 and 1 mg/mL were added to the wells. Dox was used as a reference antibiotic, and a bacterial culture without treatment was used as a negative control. The plates were incubated at 37 °C for 24 h. Following the incubation period, the wells were washed, dried, stained with 100 μL of 1% crystal violet (CV), and incubated at room temperature for 15 min. After washing, the biofilms appeared as purple rings around the periphery of the wells. To de-stain the wells, 100 μL of 95% ethanol was added. An ELISA microplate reader was used to detect the absorbance at 595 nm.

The following formula was employed to calculate the % inhibition of biofilm formation:

$$\% \text{ Inhibition} = \frac{\text{O.D.(negativecontrol)} - \text{O.D.(treatedsample)}}{\text{O.D.(negativecontrol)}} \times 100 \tag{1}$$

A similar experiment was performed for the pre-formed biofilm destruction. The same steps were carried out with only one difference: the bacteria were incubated in NB for 24 h before treatment [23]. All experiments were repeated at least three times.

2.5. 1,1, Diphenyl 1-2 Picrylhydrazyl (DPPH) Free Radical Scavenging Assay for Detecting the Antioxidant Activity of the Doped AgNPs

The test was performed by mixing 1 mL of 0.3 M of 1,1, diphenyl 1-2 picrylhydrazyl DPPH with 1 mL of the prepared doped AgNPs at different concentrations ranging between 0 and 200 µg/mL. Ascorbic acid was used as a reference positive control; 1 mL of each DPPH and methanol (95%) served as a negative control (blank). The tubes were left in the dark for 30 min, and the absorbance of each solution was recorded at 517 nm using a spectrophotometer. All tests were carried out in triplicate [28]. The percentage of the DPPH scavenging activity was calculated using the following equation:

$$\text{DPPH radical scavenging activity } (\%) = \frac{\text{Ac} - \text{As}}{\text{Ac}} \times 100 \tag{2}$$

Ac: absorbance of the control, As: absorbance of the sample.

2.6. Molecular Docking Simulation

Bacterial protein receptors were sourced from the Protein Data Bank (Table S1) to encompass a wide bacterial spectrum. Each structure underwent preparation by excluding ions, water molecules, and existing ligands. Hydrogen atoms were then incorporated into the receptor using Autodock Vina 1.2.5, with AgNPs in pdb format serving as the docking simulation input. Before docking, polar hydrogen atoms were introduced to the target, and Gasteiger charges were computed through Autodock tools. Subsequently, ligand-centered maps were created using the AutoGrid program with grid dimensions of 90 Å × 90 Å × 90 Å. Analysis of the 2-D hydrogen–bond interactions within the target ligand structure was carried out using Discovery Studio 4.5.

2.7. Statistical Analysis

The statistical analyses were performed in Excel software, the graphs were drawn in Origin software (64-bit edition, 2018), and the statistical significance was determined by *t*-tests.

3. Results and Discussion

3.1. Characterization of the Doped AgNPs

3.1.1. X-Ray Diffraction (XRD)

The XRD pattern validated the crystalline structure of the biosynthesized NPs produced using the PNLE, as shown in Figure 1. XRD patterns confirmed that the doped AgNPs synthesized with the aforementioned extract exhibited crystallinity. Specifically, the sample showed a clear, face-centered, cubic (FCC) structure observed in the biogenic AgNPs. This sample aligned with the (111), (200), (220), and (311) planes of the Ag phase, as documented in multiple studies [29]. Additionally, the sample featured eight clear and distinct peaks corresponding to the (111), (200), (220), (311), (222), (400), (331), and (420) planes of the face-centered, cubic structure of silver chloride (AgCl) as a secondary phase [30]. This pattern indicated the formation of Ag^0 nano-species alongside AgCl, likely due to the decomposition of AgCl under UV light irradiation [31]. Using MAUD software, the doped AgNPs' composition was determined as follows: 61.83% for the Ag phase, 35.88% for AgCl, 1.31% for AgO, 0.16% for the Y phase, 0.10% for the Gd phase,

and 0.72% for the Cr phase. The lattice constant for the doped AgNPs was found to be 4.085 Å, comparable to that achieved with *Sargassum algae* [32] yet surpassing that obtained using *Terminalia arjuna* leaf extract, which was 4.07 Å [33]. Furthermore, as determined using MAUD software, the average crystallite size of the biosynthesized doped AgNPs was 8.29 nm. This size was notably consistent with those of AgNPs synthesized using the green method with *Flacourtia jangomas* fruit extract, which also had a size of 8.29 nm [34]. However, this measurement was smaller when compared to that obtained through green synthesis with *Chlorella vulgaris*, which yielded a larger size of 18.94 nm [35]. This result showed that as dopants were introduced to the sample, the size of the crystallites (D) observed decreased, which may have affected the material's optical, electronic, and magnetic properties. This occurred because dopants could disturb the regular arrangement of atoms within the crystal lattice, leading to decreased crystallinity. Additionally, the average crystallite size of the biosynthesized silver chloride (AgCl) NPs was found to be 20.13 nm, smaller than the 28.6 nm size observed with *Pulicaria vulgaris Gaertn* [30]. The doped AgNPs had micro-strain values of 0.011, indicating that they had a higher level of micro-strain compared to those produced through *Pedalium murex* leaf extract green synthesis, which had a micro-strain of 0.003 [36]. This implied that doping led to a decrease in the crystallite size and an increase in the micro-strain of the doped NPs [37].
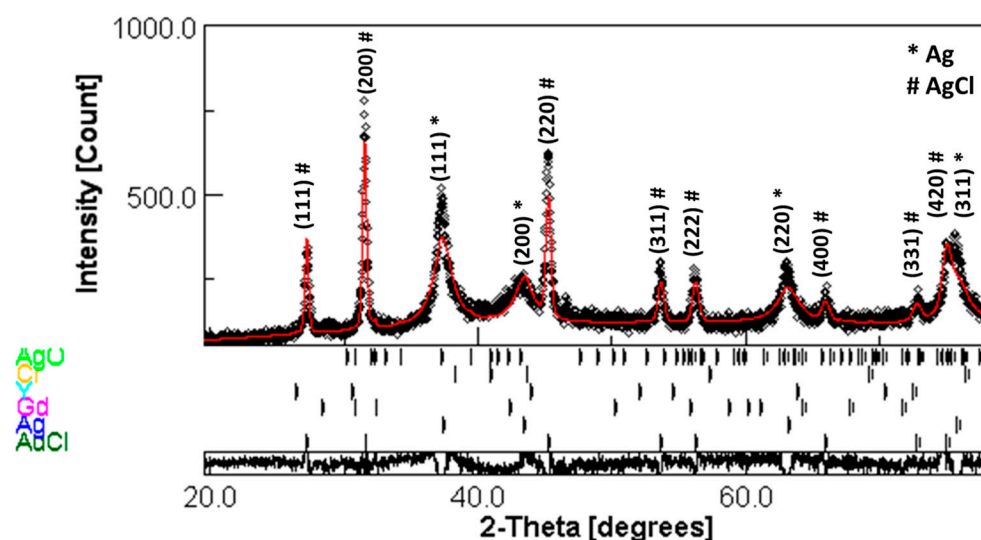
Figure 1. Doped AgNP refinement on MAUD software.

3.1.2. Transmission Electron Microscopic (TEM) Analysis

Morphological analysis of the biosynthesized doped NPs was carried out at a resolution of 100 nm using transmission electron microscopy (TEM). Figure 2a showcases TEM images of the doped AgNPs synthesized using the PNLE. Most of these NPs were spherical, though some exhibited irregular forms and were slightly agglomerated. This was consistent with a previous study on AgNPs with root extract of *Rubus ellipticus* [38]. This variation in size among the biosynthesized NPs may be attributable to the variety of reducing agents in the aqueous PNLE obtained from different parts of the pine needle leaves. The capacity of organic compounds to reduce Ag ions significantly affects NP size and distribution [39]. The dimensions of the synthesized NPs measured using ImageJ software presented in Figure 2b show that the average size of the doped AgNPs was 26.43 nm, greater than the size of 18 nm that was achieved with *M. oleifera* leaf extract. Interestingly, the sizes derived from TEM analyses of the biosynthesized NPs were larger than those obtained through X-ray diffraction (XRD) [40]. The discrepancy between XRD and TEM measurements indicated the difference between the crystallite and particle sizes. This difference may refer to the role of proteins, carbohydrates, flavonoids, and phenols in the capping and reduction of NPs, facilitating their size regulation [41].
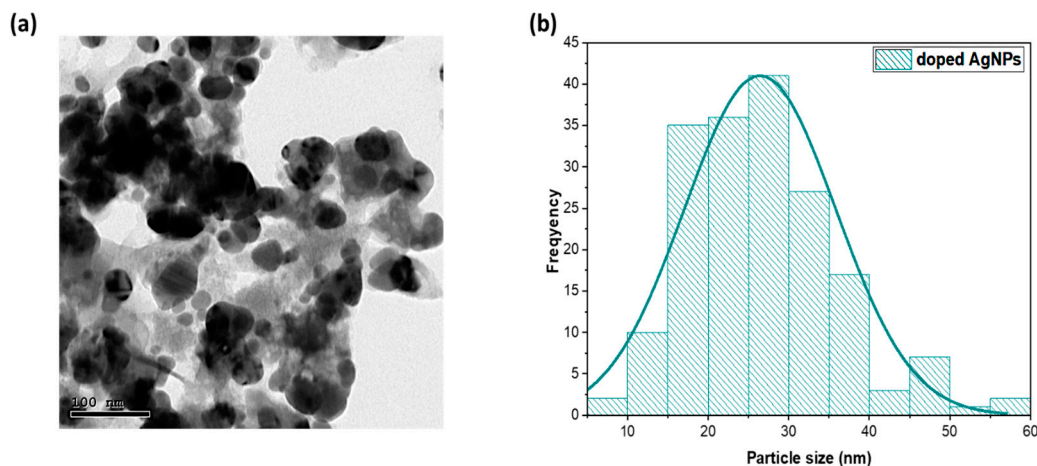
Figure 2. (**a**) TEM image and (**b**) particle size distribution graph of the doped AgNPs.

3.1.3. X-Ray Photoelectron Spectroscopy (XPS)

The X-ray photoelectron spectroscopy (XPS) method was employed to analyze the electronic structure, elemental composition, and chemical state of the synthesized NPs. The XPS survey spectrum of the doped AgNPs is shown in Figure 3a. The doped AgNP sample revealed the presence of Ag, oxygen (O), carbon (C), chlorine (Cl), nitrogen (N), yttrium (Y), gadolinium (Gd), and chromium (Cr), as shown in Table 1. Core-level spectra were taken for the sample to perform a detailed analysis of their binding environments. The HR-XPS spectra for Ag-3d of the doped AgNP sample, as shown in Figure 3b, showed the splitting of Ag-3d$_{3/2}$ and Ag-3d$_{5/2}$ peak pairs into two peaks at 374.08/376.06 eV and 368.01/370.10 eV, respectively, where the peaks at 374.08 and 368.01 eV were indicative of metallic Ag [42]. Regarding Ag-3d, the spin energy separation was aligned to the metallicity properties of metallic Ag as a doublet split separated by an energy difference of about 6.0 eV [43]. Furthermore, the HR-XPS spectrum of O-1s for the doped AgNPs, shown in Figure 3c, unveiled three principal peaks at energies of 531 eV, 532 eV, and 535 eV. The peak around 531 eV was the primary reason for the adsorbed O. However, the various peaks in this energy range showed the significant role of metal–oxygen bonds. Moreover, an important feature was the peak detected at 532 eV, which was attributed to oxygen species linked to the carboxylic group (C=O). Furthermore, the peak at 535 eV corresponded to residual H$_2$O within the NPs observed in the doped samples [44]. The HR-XPS analysis of Y-3d for the doped sample showed two peaks, the Y-3d$_{5/2}$ peak at 157.82 eV and the Y-3d$_{3/2}$ peak at 159.77 eV, as illustrated in Figure 3d [45]. The presence of Y-3d with a binding energy of about 160 eV in the doped AgNPs was notably detected, indicating the existence of Y ions. This finding is consistent with previous studies using the leaf extract of the *Liriope platyphylla* plant as a reducing agent [46]. In addition, the HR-XPS spectrum for Gd-4d is displayed in Figure 3e. Two prominent peaks were detected at binding energies of 141.8 eV and 147.97 eV, which corresponded to Gd-4d$_{5/2}$ and Gd-4d$_{3/2}$, respectively, signifying the presence of the oxidized Gd^{3+} state [14], which aligns well with recent values [47]. Additional peaks were observed at 144.5 and 153.2 eV. The splitting into different energy levels may have been due to electrostatic interaction between a partially filled core and 4*f* levels. Furthermore, Figure 3f presents the HR-XPS spectra for Cr-2p in the doped sample. For instance, the binding energies for the Cr-2p$_{3/2}$ and Cr-2p$_{1/2}$ peaks were at 572.7 eV and 583.9 eV, respectively, corresponding to the Cr-N state [41,42]. Additionally, the Cr-O states occurred at the binding energies for the Cr-2p$_{3/2}$ and Cr-2p$_{1/2}$ peaks at 576.6 eV and 586.3 eV, respectively [48]. The differences in elemental composition for the doped AgNP samples were primarily composed of Ag (5.96%), O (70.27%), Gd (3.38%), Cr (3.15%), N (13.06%), and Cl (4.17%). The presence of chloride in the sample was consistent with the formed AgCl phase. These changes in the elemental composition are consistent with the literature, suggesting that doping improves the stability of AgNPs through modification of

the surface chemistry. The introduction of dopants such as Gd, Cr, and Y has been reported to enhance their antibacterial and catalytic activity, among other functions in applications.
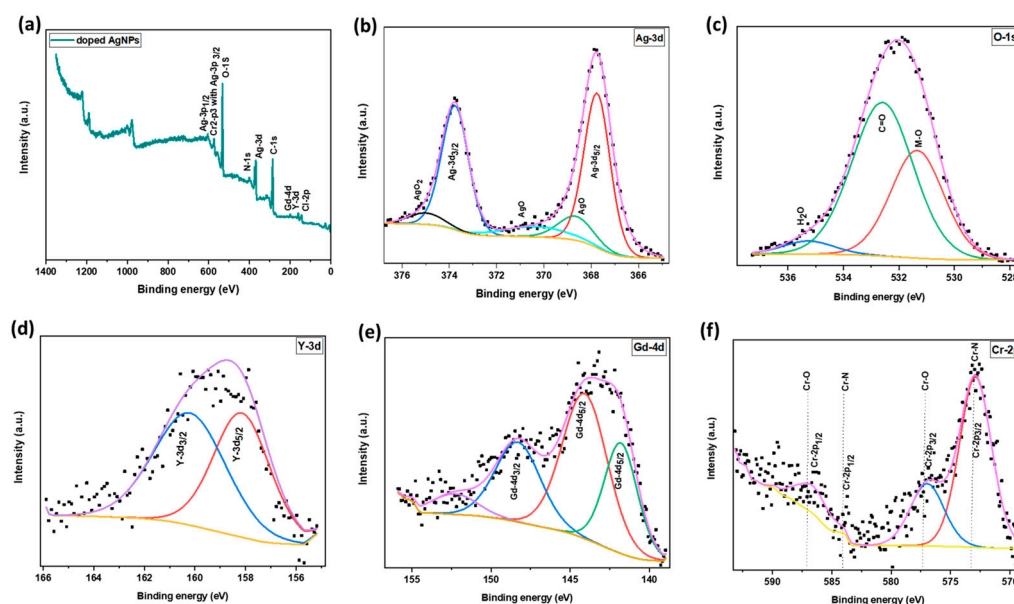
Figure 3. XPS spectrum of the doped AgNPs. (**a**) Survey spectrum, (**b**) HR- XPS of Ag-3d, (**c**) HR-XPS of O-1s, (**d**) HR-XPS of Y-3d, (**e**) HR-XPS of Gd-4d, and (**f**) HR-XPS of Cr-2p.The squares in (**b**–**e**,**f**) refer to the experimental data, the purple solid line refers to the envelope, the yellow solid line refers to the background, the blue, red, green, black, and cyan solid lines refer to different spectral lines indicated in the figure.

Table 1. Elements in the doped AgNPs and their atomic percentage.

Elements	Atomic Percentage
Ag-3d	5.96
O-1s	70.27
Gd-4d	3.38
Cr-2p3	3.15
N-1s	13.06
Cl-2p	4.17

3.1.4. Scanning Electron Microscopy (SEM) with Energy-Dispersive X-Ray (EDX) Spectroscopy Analysis

The SEM micrograph in Figure 4a shows the spherical morphology of the particles synthesized by the green method. The EDX spectrum shown in Figure 4b revealed the presence of silver (Ag), yttrium (Y), gadolinium (Gd), chromium (Cr), oxygen (O), chlorine (Cl), and carbon (C) elements. The atomic % of the presented elements is listed in the inset of Figure 4b. The EDX spectrum exhibited elemental signals of silver atoms in the biosynthesized doped AgNP samples at around 3 keV. According to earlier observations, Ag-NPs frequently exhibit an absorption peak of almost 3 keV in their EDX pattern. Due to the synthesis of nanoparticles using biomaterials and green plants, carbon and oxygen elements are possible [49]. However, the highest percentage of a silver element was shown in the EDX analysis, indicating that Ag nanoparticles made up the majority of the product [49]. Apart from the Ag peaks, there were weaker signals of O (0.52 keV), C (0.28 keV), and Cl (2.62 keV). These weaker signals were probably due to X-ray emission from enzymes or proteins in the extract. Moreover, the presence of C, O, and Cr peaks in the EDX spectra supported chromium reduction from the precursor [50]. In addition,

C traces may have originated from the C tape utilized in sample preparation [17]. Moreover, the presence of Y due to doping silver with yttrium, gadolinium, and chromium nanoparticles affected their optical and structural properties [51]. Gd had a characteristic X-ray peak at 6.056 keV in the EDX analysis. These findings could be explained by the proteins and flavonoids in the pine needle leaf extract used in the green synthesis process, which may have helped cap the silver nanoparticles. This result aligns with previous research findings demonstrating that silver nanoparticles synthesized using seed extract from *Alpinia katsumadai* validate the role of plant constituents, including proteins and flavonoid compounds, in capping silver nanoparticles and preventing their aggregation.
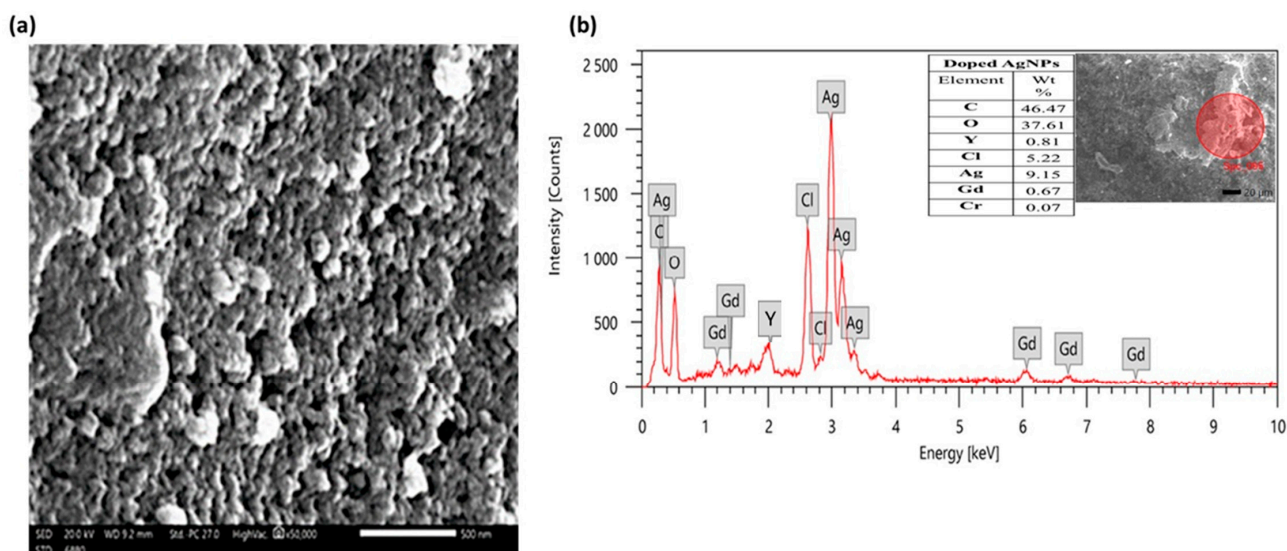

Figure 4. (**a**) SEM image and (**b**) EDX spectrum for green synthesized doped AgNPs, with insets of atomic % and selected scanning area.

3.1.5. Fourier Transform Infrared (FTIR) Analysis

The synthesized doped AgNPs were analyzed by Fourier transform infrared (FTIR) spectroscopy in the spectral range of 4000–400 cm^{-1} at room temperature for the qualitative assessment of chemical bonding through infrared light scanning. This identification was essential for understanding the functional groups required in NP synthesis and the wavelength absorbance of specific functional groups such as ketones, alkanes, and amines. It aided in biomolecule identification [52]. As shown in Figure 5, the O-H stretching observed at 3377.74 cm^{-1} for the doped AgNPs indicated the possible influence of alcoholic or phenolic stretching and highlighted the importance of the polyphenolic extract components in NP stabilization [34]. The peak at 2921.79 cm^{-1} was caused by the C-H stretching of alkenes. Also, the peak at 2366.62 cm^{-1} aligned carbonyl bond (O=C=O) stretching, indicating carbonyl-containing groups' role in Ag ion bio-reduction. The intense band at 2366.62 cm^{-1} highlighted N-H stretching, showcasing the subtle differences in chemical bonding. Moreover, the doped AgNP samples exhibited bands at 1643.84 cm^{-1}, suggesting the presence of carbonyl groups from green synthesis reducing agents, thus supporting the role of organic compounds in NP stabilization [8]. On the other hand, the bands at 1535.39 cm^{-1} indicated nitro molecule (N-O) stretching. The bands at 1410.49 cm^{-1} were linked with O-H in carboxylic acids [53]. Additionally, smaller bands were observed near 1235.96 cm^{-1}, attributed to the C-N stretching of amines [54]. The peak at 1077.32 cm^{-1} corresponded to C-O stretching from different organic compounds [55]. Correspondingly, metal–oxygen (M-O) stretching vibrations existed in the range of 500–700 cm^{-1}; specifically, Y-O stretching was observed at 695.83 cm^{-1} for the doped AgNPs. These vibrations indicated a complicated interaction of hydroxide and nitrate with yttrium ions, alongside probable Ag-O vibrations at 541.99 cm^{-1}, representing the complex chemical dynamics involved during nanoparticle synthesis [56]. Thus, organic

phytochemicals identified through XPS analysis confirmed the FTIR data collected during the characterization studies.
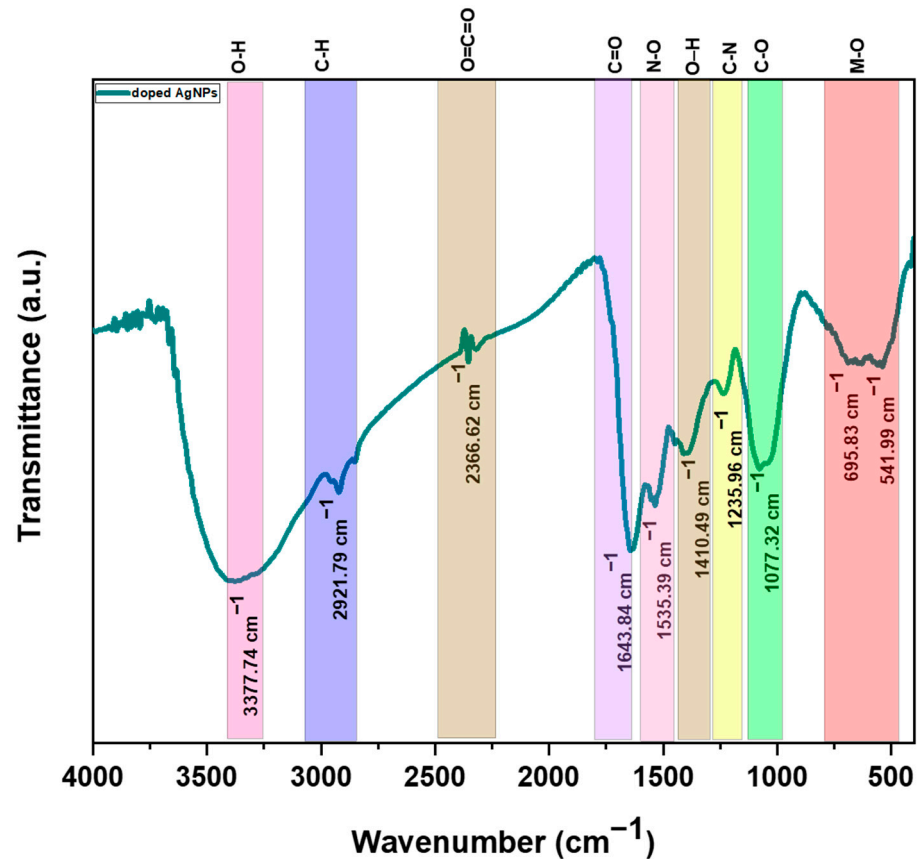
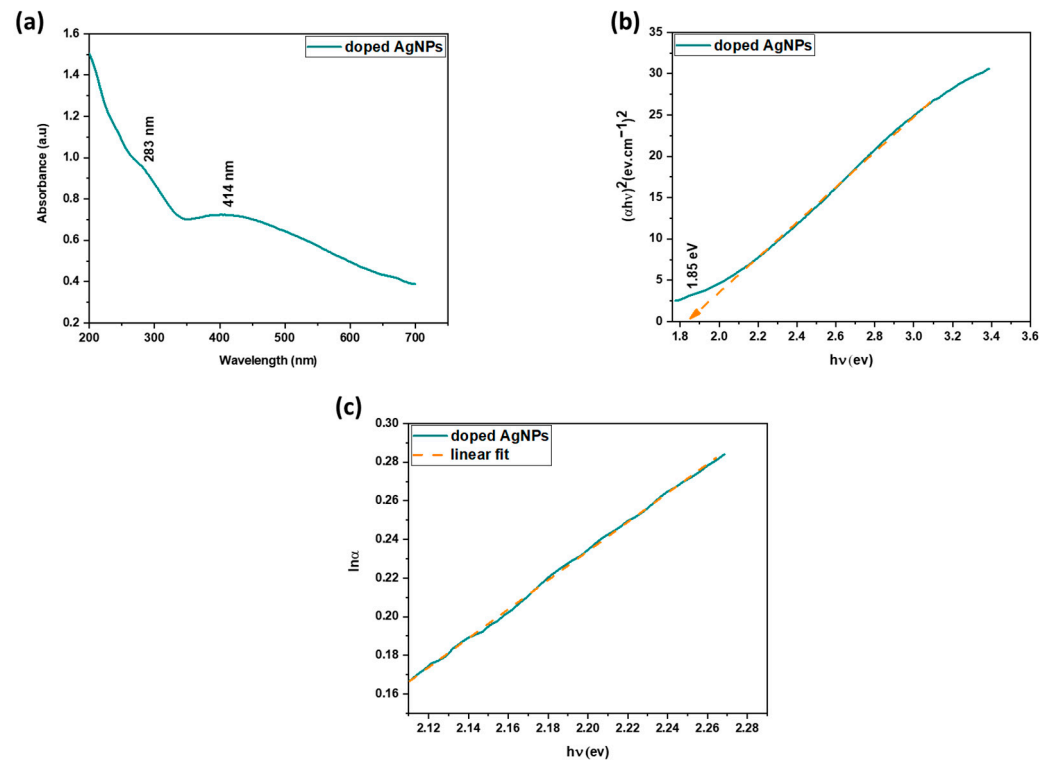**Figure 5.** FTIR spectrum for green synthesized doped AgNPs.

3.1.6. Visual Observation and UV–Vis Spectroscopy Analysis

The optical absorption spectra of the samples obtained were analyzed using UV–vis spectrum analysis within the 200–700 nm wavelength range to assess the initial presence of metal NPs in the plant-based aqueous medium. As illustrated in Figure 6a, the doped AgNPs showed two absorption peaks at 283 nm and 414 nm, with a strong SPR band at 414 nm caused by the excitation of the metal's free electrons during NP formation [57]. Additionally, the absorption band in the UV region was suggestive of certain plant polyphenols and flavonoids, exclusive of other phytochemicals in the extract itself [58]. Notably, the UV absorption spectrum showed a distinct peak at about 283 nm, which likely corresponded to the presence of doped elements, aligning with previous research on rare earth oxides [59]. Additionally, the direct band gap (E_g) value for the green synthesized doped AgNPs was obtained from the absorbance spectrum using the Tauc's plot method, which is a theoretical correlation between the absorption coefficient (α) and the photon energy (hv) [17]:

$$(\alpha hv)^n = B(hv - E_g) \tag{3}$$

The absorption coefficient (α) was calculated using the measured absorbance (A):

$$\alpha = 2.303\left(\frac{A}{t}\right) \tag{4}$$

Figure 6. (**a**) UV–visible spectrum, (**b**) band gap energy calculations and the dashed line represent the extrapolation for the linear fit, and (**c**) Urbach energy plot of green synthesized doped AgNPs.

In the equations, t denotes the path length, B is a constant, and n is an exponent with a value of 2 for the direct bandgap transition, as illustrated in Figure 6b [17]. The direct bandgap was calculated from the Tauc's plot, determined by extrapolating the linear segment of the Tauc's plot curves $(\alpha h v)^2$ versus the photon energy $h v$ to y = 0, as illustrated in Figure 6b. The doped AgNPs demonstrated a direct bandgap value of 1.85 eV, which was lower than the 3.39 eV observed in AgNPs synthesized using garlic leaf extract [60]. This reduction in the energy gap with silver doping was attributed to the alteration in the grain size of the sample due to doping [49]. Moreover, the presence of a tail further indicated structural defects in the NPs. The Urbach energy (E_u) denotes the width of the band tails of localized states. The slope of the linear portion of the plot of $ln\alpha$ against photon energy (Figure 6c) is used to calculate the Urbach energy according to Equation (5) [17]:

$$\alpha = \alpha_0 \exp\left(\frac{h v}{E_u}\right) \tag{5}$$

In the equation, α_0 represents a constant. Figure 6c depicts the change in $ln\alpha$ with respect to $h v$. The values of E_u of the doped AgNP samples were derived from the reciprocal slope of the linear segment in the tail region, which was equivalent to 1.32 eV.

3.1.7. Photoluminescence (PL) Studies

To investigate the optical properties of the doped AgNPs, the photoluminescence (PL) spectrum was studied at room temperature under excitation of 420 nm. The PL emission was visible from 450 to 700 nm and exhibited five different emission peaks at 456.83 nm, 476.44 nm, 513.15 nm, 575.51 nm, and 619.74 nm. This visible luminescence was attributed to electron excitation from occupied d bands to states above the Fermi level [61]. Before recombination, electron–phonon and hole–phonon scattering resulted in energy loss that affected the photoluminescent behavior [62]. To elucidate the broad emission observed, a Voigt fitting analysis was used to deconvolute the photoluminescence (PL) curve of the doped AgNPs into five different components, as shown in Figure 7. The samples showed

two blue emissions at 456.83 nm and 476.44 nm due to the recombination of electrons in Ag vacancies with valence band holes. These emissions were caused by interactions between the NPs [63]. Furthermore, a green emission at 513.15 nm indicated the presence of O vacancies. Additionally, the yellow emission (575.51 nm) suggested some defect states, such as those created by O vacancies or impurities in dopants used during the synthesis process. Finally, the red emission peak at 619.74 nm correlated with surface defects attributed to the small sizes of the bio-synthesized doped AgNPs [64]. Furthermore, the introduction of dopants created band levels that served as traps for charge carriers, effectively lowering the recombination rate of electrons and holes and thereby improving the optical behavior of the NPs [65].
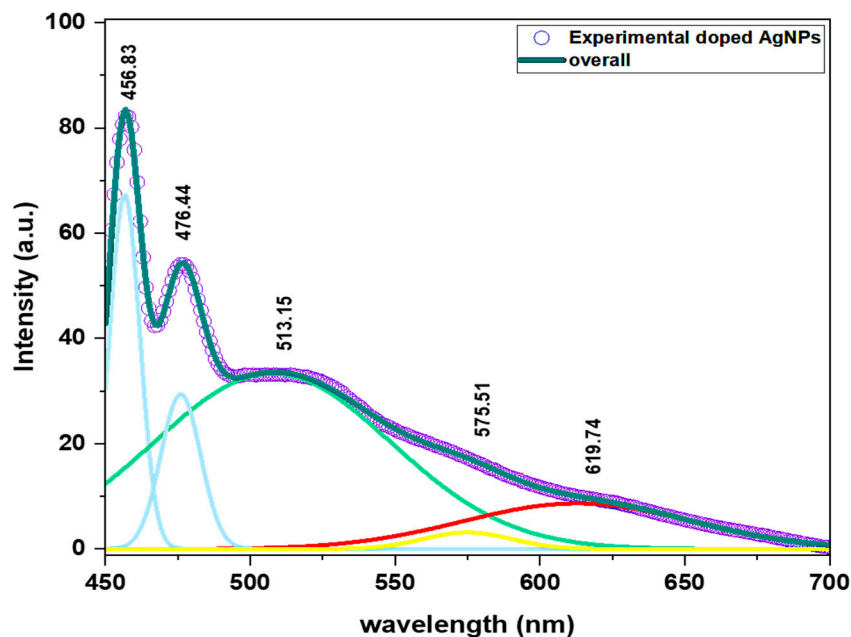
Figure 7. PL spectrum for the green synthesized doped AgNPs. The dots represent the experimental data, the dark cyan solid line represents the overall fitting of the spectra, the blue, green, yellow, and red lines represent the deconvolution for the PL spectra referring to different transitions.

3.1.8. Vibrating Sample Magnetometer (VSM)

A vibrating sample magnetometer (VSM) was used to study the magnetic properties of the doped AgNPs at room temperature in a magnetic field range from -20 to $+20$ kG (Figure 8a). According to the hysteresis loops, doped AgNPs showed a weak ferromagnetic tendency, which was also supported by a slight increase in magnetization with the applied field. The weak ferromagnetic nature may have arisen due to different factors. The interaction between capping agents and the Ag surface appeared to play a role in generating weak ferromagnetism [66]. A trace amount of O, indicative of a possible non-stoichiometric oxide layer on the NPs, could also have contributed to their ferromagnetism. Additionally, incorporating rare earth elements into the structure of the doped AgNPs was responsible for their improved ferromagnetic activity. A range of magnetic metrics such as the magnetization at 20 kOe (M_{20kOe}), retentivity (M_r), coercivity (H_{ci}), and squareness ratio ($S = M_r/M_S$) were determined and are succinctly listed in Table 2. The squareness value was less than 0.5, suggesting a multi-domain structure characterized by uniform magnetization and isotropic particle distribution [67]. In addition, the saturation magnetization (M_S) was calculated using the law of approach to saturation:

$$M = M_S \left(1 - \frac{b}{H^2} \right) \tag{6}$$
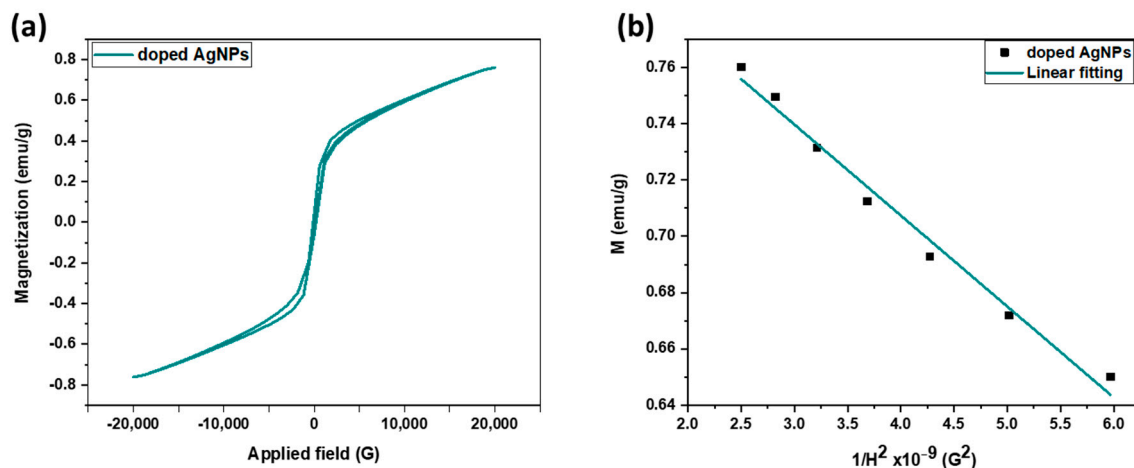
where *b* is a constant related to anisotropy.

Figure 8. (**a**) Magnetization curve and (**b**) law of approach-to-saturation curve of the doped AgNPs.

Table 2. Magnetic parameters for the doped AgNPs.

Sample	M_{20kOe} (emu/g)	M_s (emu/g)	$M_r \times 10^{-3}$ (emu/g)	H_{ci} (G)	S
Doped AgNPs	0.761	0.836	51.943	156.780	0.006

M_{20kOe}: magnetization 20 KOe, M_s: saturation magnetization, M_r: retentivity, H_{ci}: coercivity.

Moreover, as illustrated in Figure 8b, a linear regression of magnetization was denoted against the inverse square of the applied magnetic field at higher field strengths, from which the saturation magnetization (M_S) value was derived. The doped AgNPs yielded a saturation magnetization of 0.761 emu/g. This finding is consistent with prior research employing Y-doped iron oxide NPs, where it was found that increasing the doping concentration increased magnetizations up to maximum values [68]. Notably, this magnetization was higher than that of AgNPs prepared from *Artocarpus heterophyllus* leaf extract, recorded at 0.085 emu/g [69]. The curve for the doped AgNPs showed a steeper ascent to saturation, having higher saturation magnetization, implying that the dopant effectively enhanced the magnetic moments within the particles.

3.2. Antibacterial Activity of the Doped AgNPs Against Uro-Pathogenic Bacteria

3.2.1. Minimum Inhibitory Concentrations (MICs) and Minimum Bactericidal Concentrations (MBCs) of the Doped AgNPs

The results of the microwell dilution method show that the doped AgNPs responded to the bacterial isolates by processing a bactericidal effect. They exerted bactericidal activity against all isolates (MBCs ranging between 0.25 and 0.5 mg/mL), except *E. faecalis* and *K. pneumonia*, where they exerted a bacteriostatic effect (MICs ranging between 0.5 and 1 mg/mL). The MIC and MBC results are presented in Table 3 and Figures 9 and S1; it is reported that a ratio of MBC/MIC less than 4 showed a bactericidal effect of the antimicrobial agent [70]. This confirmed the bactericidal action of the doped AgNPs against all bacterial isolates. The results show that the doped AgNPs inhibited bacterial growth at moderate concentrations. This could be attributed to the agglomeration of the doped AgNPs shown by the TEM results. However, the bactericidal effect showed that doping did not decrease the antibacterial activity. In addition, *E. coli* was the most resistant bacterium to the doped AgNPs, indicating that the NPs exhibited a better inhibitory activity against Gram-positive bacteria. This result is consistent with previous studies reporting that Gram-negative bacteria are more resistant to antibacterial agents due to the presence of a lipopolysaccharide layer in addition to the peptidoglycan layer [24–27]. Furthermore, the antibacterial activity depended on the structure of the NPs and their interaction with bacterial cells. The small size of the NPs shown by TEM analysis (26.43 nm) and their crystalline structure favored their penetration into bacteria. This confirmed the significant

activity of the doped AgNPs. In addition, their functional groups, as demonstrated by the FTIR results, could interact with the different components in the cell, leading to cell lysis. Similar results were shown by previous studies reporting the antimicrobial activity of AgNPs against bacteria. For example, significant antibacterial activity of AgNPs derived from the stem bark of *Terminalia arjuna* against *E. coli* and *S. aureus* was reported. In addition, a previous review showed that AgNPs inhibited the growth of a group of bacteria, including *E. coli*, *P. aeruginosa*, *S. typhimurium*, and *B. cereus*, at MICs ranging between 50 and 200 μg/mL [71,72]. The shape of the NPs also played a vital role in the antibacterial potential. The TEM results revealed a spherical shape of the doped AgNPs. Usually, sharp-edged NPs displayed better antimicrobial activities than round-shaped NPs. However, spherical NPs had a large surface area-to-volume ratio, indicating their efficiency in the antibacterial processes [73]. When compared to undoped AgNPs, the previous literature reported significant antibacterial activity of undoped AgNPs, especially against *E. coli* and *S. aureus*. However, the MICs were relatively higher than those reported in this study (approximately 434 mg/mL) [74]. This action was due to the Ag^+ ions that the particles could release. These ions could potentially cause damage to bacterial cell walls, distort proteins, and interfere with DNA replication. Such nanoparticles would be able to specifically target multiple bacterial locations, increasing the difficulty in developing bacterial resistance [47]. Undoped AgNPs, however, are not without their challenges: agglomeration, instability, and even cytotoxicity at high concentrations have been reported. However, the future looks promising for the potential to enhance the efficacy and reduce the toxicity of doped Ag nanoparticles. Doping with metals, non-metals, and rare earth elements has increased the antibacterial activity of AgNPs. This enhancement works by mechanisms such as the enhanced generation of reactive oxygen species (ROS), which leads to oxidative stress in bacterial cells. Further, the release of Ag^+ ions may lead to better bacterial membrane interactions because the charge distribution on the nanoparticle surface may be changed, resulting in more stable membranes with improved release kinetics. Some dopants, for example, yttrium or cerium, have antibacterial activity on their own and can increase the antibacterial activity of nanoparticles [5]. Dox exerted bactericidal activity against all bacterial isolates and was able to kill bacteria at a concentration of 1.25 μg/mL. This efficiency was attributed to its ability to inhibit the 30S ribosomal subunit and, in turn, inhibit protein synthesis, leading to cell death [23,75]. Overall, the doped AgNPs exerted significant antibacterial potential against all bacterial isolates tested.

Table 3. MICs and MBCs of the doped AgNPs.

| Bacterial Isolates | MICs and MBCs of the Doped AgNPs | | | | | |
| | Doped AgNPs (mg/mL) | | | Dox (μg/mL) | | |
	MIC	MBC	MBC/MIC	MIC	MBC	MBC/MIC
S. aureus	0.25	0.5	2	ND	1.25	ND
S. haemolyticus	0.25	0.5	2	ND	1.25	ND
E. faecalis	1	>1	1	ND	1.25	ND
E. coli	0.125	0.25	2	ND	1.25	ND
K. pneumonia	0.5	>1	0.5	ND	1.25	ND
P. aeruginosa	0.25	0.5	2	ND	1.25	ND

MIC: minimum inhibitory concentration, MBC: minimum bactericidal concentration, AgNPs: silver nanoparticles, Dox: Doxycycline, ND: not determined.
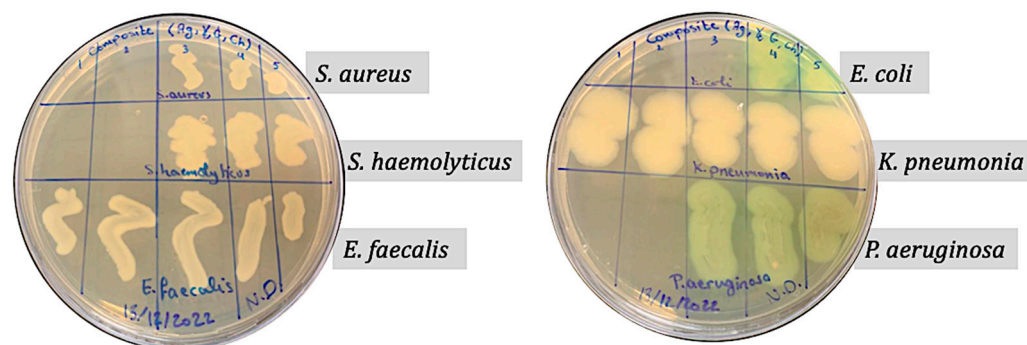
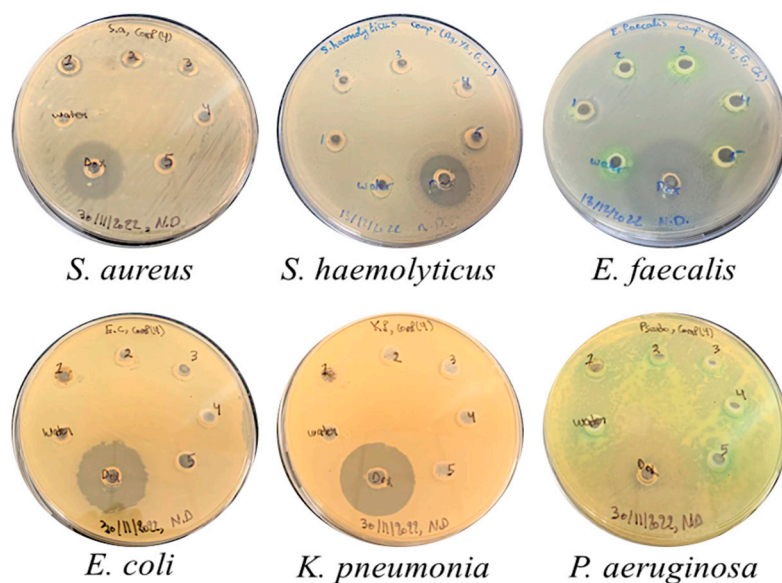**Figure 9.** MBC results of the doped AgNPs.

3.2.2. Inhibition of Bacterial Growth Induced by the Doped AgNPs Shown by the Zones of Inhibition (ZOIs) Through Agar Well Diffusion

The agar well diffusion (AWD) results confirmed the MIC and MBC microdilution assay results. The significant ZOIs ranged between 7 and 18 mm. The agar well diffusion results are presented in Table 4 and Figure 10. The best activity of the doped AgNPs was observed against *S. aureus* and *P. aeruginosa* (ZOI = 12 mm) and the worst was observed against *S. haemolyticus*, *E. coli*, and *K. pneumonia* (ZOI = 8.3 mm), thus confirming their better activity against Gram-positive bacteria. The results were attributed to the structure and interaction between the NPs and the bacterial cells. As reported in the previous literature, the antibacterial activity of NPs relies on many unelucidated mechanisms. These include the penetration of the cell wall, generation of reactive oxygen species (ROS), alteration of the production of specific secondary metabolites that aid in the protection against antibacterial agents, induction of oxidative stress in the bacterial cells, and interruption of the internal electron flow, thus leading to membrane damage and, eventually, cell death [24–27,73]. For Dox, the ZOIs ranged between 15 and 30 mm. Based on the Clinical and Laboratory Standards Institute (CLSI), all bacteria are considered sensitive to Dox in this range [76]. However, the most sensitive bacterium was *S. haemolyticus*, explaining the fact that Gram-positive bacteria are more sensitive to antibacterial drugs due to the absence of an outer protective membrane [77]. Overall, the AWD results confirmed the use of the doped AgNPs as potential antibacterial agents against uro-pathogenic bacteria.

Table 4. ZOIs of the doped AgNPs against the bacterial isolates.

NPs		Bacterial Isolates					
		Gram-Positive			Gram-Negative		
		S. aureus	*S. haemolyticus*	*E. faecalis*	*E. coli*	*K. pneumonia*	*P. aeruginosa*
Sample	Concentration	ZOI ± SEM (mm)					
Doped AgNPs (mg/mL)	0.0625 *p*-value Significance	7.3 ± 0.27 <0.001 ***	8.0 ± 0.00 0.002 **	7.0 ± 0.00 <0.001 ***	0.0 ± 0.00 0.001 ***	0.0 ± 0.00 <0.001 ***	9.3 ± 0.27 0.003 **
	0.125 *p*-value Significance	8.3 ± 0.27 <0.001 ***	8.0 ± 0.00 0.002 **	7.3 ± 0.27 <0.001 ***	0.0 ± 0.00 0.001 ***	7.0 ± 0.00 0.001 ***	9.3 ± 0.27 0.003 **
	0.25 *p*-value Significance	9.3 ± 0.27 0.001 ***	8.3 ± 0.27 <0.001 ***	8.0 ± 0.00 <0.001 ***	8.0 ± 0.00 0.003 **	7.3 ± 0.27 <0.001 ***	10.3 ± 0.00 0.005 **
	0.5 *p*-value Significance	11.3 ± 0.27 0.001 ***	8.3 ± 0.27 <0.001 ***	10.3 ± 0.27 <0.001 ***	8.3 ± 0.27 0.001 ***	7.3 ± 0.27 <0.001 ***	11.0 ± 0.00 0.02 *
	1 *p*-value Significance	12.0 ± 0.00 0.006 **	8.3 ± 0.27 <0.001 ***	12.0 ± 0.00 0.001 ***	8.3 ± 0.27 0.001 ***	8.3 ± 0.27 <0.001 ***	12.0 ± 0.00 0.03 *
Dox (μg/mL)	1.25 *p*-value Significance	19.0 ± 0.47 <0.001 ***	20.0 ± 0.47 <0.001 ***	30 ± 0.47 <0.001 ***	18 ± 0.47 <0.001 ***	20 ± 0.47 <0.001 ***	15 ± 0.47 <0.001 ***

AgNPs: silver nanoparticles, ZOI: zone of inhibition, SEM: standard error of the mean, Dox: Doxycycline; *p*-values were calculated as follows: * $p < 0.05$, ** $p < 0.01$, *** $p < 0.001$.

Figure 10. Agar well diffusion results of the doped AgNPs at different concentrations (0.0625–1 mg/mL) against the bacterial isolates.

3.2.3. Time–Kill Results of the Doped AgNPs Against Bacterial Isolates

The time–kill results in Table 5 and Figure S2 reveal that the doped AgNPs needed about 3 h to inhibit bacterial growth at MICs. All bacterial isolates took 3 h to be inhibited. The bacteria usually need this time to adapt to their medium and start duplicating [78]. This suggests that the NPs limited the adaptation and duplication of bacteria. A probable mechanism reported previously includes limiting nutrient uptake by the bacterium from the medium due to the interaction of the NPs with the bacterial components [78,79]. This leads to changes in the bacterial conformation, which prevents their adaptation, decreases their metabolic reactions, and, eventually, leads to bacterial cell lysis. Regarding Dox, it exerted its bactericidal effect after 2 h of its incubation with the bacterial isolates. This result was similar to that of the doped AgNPs, meaning that Dox worked in a similar way to the NPs by preventing the attachment of the bacteria by preventing nutrient uptake from the medium, in addition to the inhibition of protein synthesis.

Table 5. Time of inhibition of bacterial growth marked by the doped AgNPs.

| Bacterial Isolates	Time of Inhibition of Bacterial Growth (h)	
	Doped AgNPs	Dox
S. aureus	3	2
S. haemolyticus	3	2
E. faecalis	3	2
E. coli	3	2
K. pneumonia	3	2
P. aeruginosa	3	2

AgNPs: silver nanoparticles, Dox: Doxycycline.

3.2.4. Inhibition of Biofilm Formation and Eradication of Pre-Formed Biofilms by the Doped AgNPs

Inhibition of Bacterial Biofilm Formation by the Doped AgNPs

An antibiofilm formation assay was performed to reveal the ability of the doped AgNPs to prevent the formation of bacterial biofilms. Inhibitory percentages above 10% were considered effective, and negative percentages showed the enhancement of biofilm formation [80]. The results presented in Figure 11a show that the doped AgNPs inhibited the formation of all bacterial biofilms at concentrations ranging between 0.5 and

1 mg/mL, with the best effect against *E. faecalis* (75.6% inhibition) and the worst effect against *K. pneumonia* (43.9% inhibition). The impact on biofilms was less than that on the bacterial isolates. This was attributed to the ability of biofilms to secrete particular proteins and exopolysaccharides, which increased their resistance to antibiofilm agents [24,78,80]. The antibiofilm action depended on the constituents of the NPs and their interaction with bacteria inside the biofilm. The previous literature reported that the primary chemical reaction taking place between NPs and biofilms is the interaction with the secreted proteins, preventing the attachment of the cells to the surface, known as the first stage of biofilm formation [24,78–81]. Overall, the doped AgNPs exerted significant antibiofilm activities, making them effective against infectious biofilms, especially in the urinary tract.
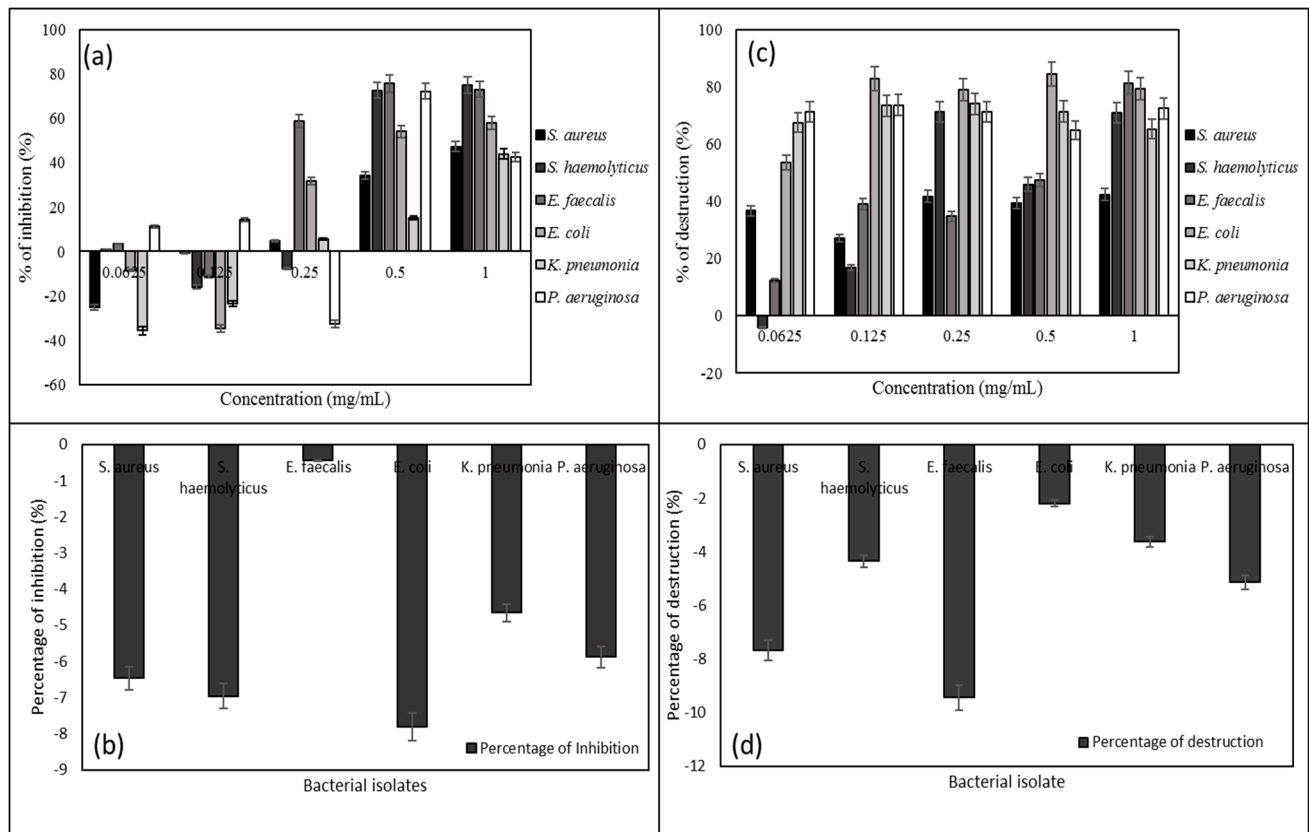
Figure 11. Inhibition of biofilm formation by the (**a**) doped AgNPs and (**b**) Dox and destruction of the pre-formed bacterial biofilms by the (**c**) doped AgNPs and (**d**) Dox.

Destruction of Pre-Formed Bacterial Biofilms by the Undoped and Doped AgNPs

Similar to the inhibition of biofilm formation results, the doped AgNPs significantly inhibited pre-formed biofilms. The results presented in Figure 11b report that the doped Ag-NPs caused the destruction of all biofilms at concentrations ranging between 0.125 and 1 mg/mL, with the best action against *E. coli*, with 84.4% of biofilm destruction, and the lowest action against *S. aureus*, with 42.3% of biofilm destruction. This indicated a better effect of the doped AgNPs against Gram-negative biofilms. The action observed can be explained by the ability of the NPs, due to their small size, to penetrate the biofilm cells and prevent their attachment, enhancing their dispersion. This led to morphological changes in the cells of the biofilms, causing complete lysis, thus destroying the pre-formed biofilms [24,27,28,78]. It is worth mentioning that the antibiofilm effects were concentration-independent, meaning that the inhibitory and destructive concentrations were different from the MICs of the doped AgNPs. This could be attributed to the absorbance and enumeration of cells [23,81]. When a biofilm was formed, the number of attached cells increased. This means that higher concentrations than the MICs were needed to destroy the formed

biofilms. Thus, the absorbance and cell enumeration were different from those of single isolates. For Dox, the bacterial biofilms were neither inhibited nor destroyed. This result is normal since antibiotics are still not classified as biofilm treaters. None of the antibacterial drugs presented up to now could cope with the biofilms.

3.3. Antioxidant Activity of the Doped AgNPs Against DPPH by Radical Scavenging Assay

The antioxidant results show that the doped AgNPs exerted significant activity, with a scavenging percentage reaching 61.3% (Figure 12). The reported results are consistent with those of the previous literature [82]. For example, Bedlovicova et al. demonstrated the antioxidant action of AgNPs, which reached 64.5%, similar to our results [82]. The antioxidant action was attributed to the presence of phytochemicals, particularly polyphenols and flavonoids, that acted as catalysts for the antioxidant reactions. In addition, the adsorption of bioactive compounds played a vital role in the antioxidant activity. The NPs acted as oxygen quenchers, hydrogen donors, and reducing agents, which increased the antioxidant potential. Another antioxidant mechanism relied on hydrogen peroxide in the NPs, which induced ROS, leading to increased toxicity, thus enhancing the antioxidant activity [82]. The doped AgNPs could be classified as effective antioxidant agents.
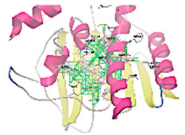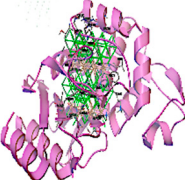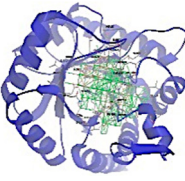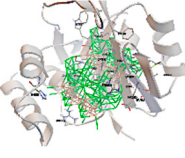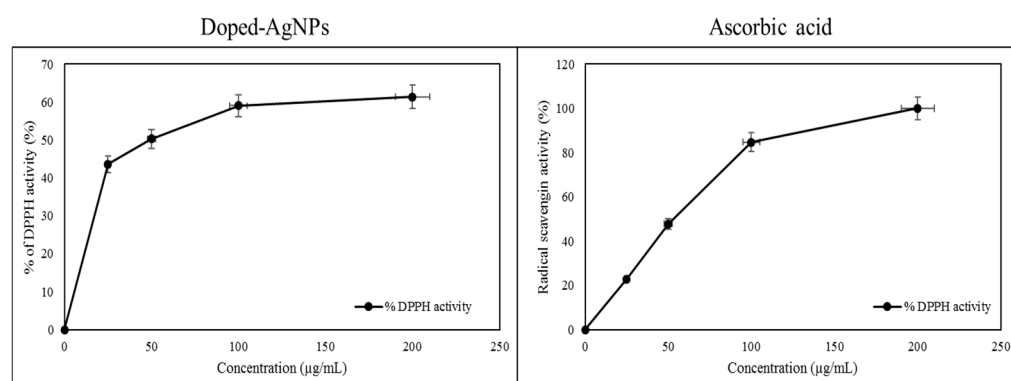

Figure 12. Antioxidant activity of the doped AgNPs and ascorbic acid against DPPH.

### 3.4. Molecular Docking of Doped AgNPs with Antibacterial Target Proteins

DNA gyrase serves as a pivotal enzyme involved in replication and repair. The findings from the docking outcomes (Table 6) indicate that the doped AgNPs exhibited an affinity interaction of −9.80 kcal/mol. The doped AgNPs formed two hydrogen bonds with Ser73 and Glu42. Additionally, hydrophobic connections with the doped AgNPs comprised six metal–acceptor bonds with Glu42, Met166, Ser70, Asp73, Glu42, and Gln143, along with a Pi–Sigma bond with Phe169 (Figure 13A–C). These results align with those of Siddique et al. (2024), who utilized molecular docking simulations against DNA gyrase to elucidate the mechanism underpinning the observed antibacterial properties [83]. Also, in silico molecular docking investigations revealed that AgNP nanostructures had strong antibacterial action against DNA gyrase *E. coli* [17].

Penicillin-binding proteins (PBPs) represent a group of enzymes discovered in *E. faecalis* that hold significance in the construction of cell walls. The doped AgNPs unveiled affinity interactions amounting to −10.22 kcal/mol. Notably, the doped AgNPs established three hydrogen linkages with Ile516, Thr519, and Ile547. In addition, hydrophobic associations with the doped AgNPs encompassed a carbon–hydrogen bond with Ser367, alongside nine metal–acceptor bonds with Thr651, Gln551, Ser367, Tyr420, Thr418, Val369, Leu650, Ile550, and Val382 (Figure 13D–F). These discoveries resonated with the research conducted by Ikram et al. (2024) [84], who utilized in silico docking to demonstrate the potential of synthesized nanomaterials in impeding PBP, crucial for cell wall synthesis [84].

Table 6. Molecular interactions of the doped AgNPs with amino acids of the antibacterial protein targets.

Bacteria	3D Structure	Hydrophilic Interactions		Hydrophobic Contacts		No. of H-Bonds	No. of Total Bonds	Affinity kcal mol^{-1}
		Residue (H-Bond)	Length	Residue (Bond Type)	Length			
1 *E. coli*		Ser73 (H-Bond) Glu42 (H-Bond)	2.33 2.55	Glu42 (Metal–Acceptor) Met166 (Metal–Acceptor) Ser70 (Metal–Acceptor) Asp73 (Metal–Acceptor) Glu42 (Metal–Acceptor) Gln143 (Metal–Acceptor) Phe169 (Pi–Sigma)	2.62 2.09 3.21 2.36 1.18 2.95 3.90	2	9	−9.80
2 *E. faecalis*		Ile516 (H-Bond) Thr519 (H-Bond) Ile547 (H-Bond)	3.22 261 3.00	Ser367 (C-H-Bond) Thr651 (Metal–Acceptor) Gln551 (Metal–Acceptor) Ser367 (Metal–Acceptor) Tyr420 (Metal–Acceptor) Thr418 (Metal–Acceptor) Val369 (Metal–Acceptor) Leu650 (Metal–Acceptor) Ile550 (Metal–Acceptor) Val382, (Metal–Acceptor)	2.11 3.10 4.25 1.95 2.44 3.15 4.80 2.11 2.00 3.50	3	13	−10.22
3 *K. pneumonia*		-	-	Leu148 (Metal–Acceptor) Met152 (Metal–Acceptor) Tyr247(Metal–Acceptor) Thr235 (Metal–Acceptor) Gly232 (Metal–Acceptor) Arg161 (Metal–Acceptor) Thr180 (Metal–Acceptor) Asp157 (Metal–Acceptor) Phe66 (Metal–Acceptor)	3.26 3.34 2.87 2.11 2.85 2.90 3.12 2.54 3.26	0	9	−10.20
4 *P. aeruginosa*		Lys34 (H-Bond) Gly126 (H-Bond)	2.11 3.22	Phe51 (Metal–Acceptor) Gly38 (Metal–Acceptor) Ser129 (Metal–Acceptor) Lys34 (Metal–Acceptor) Gly126 (Metal–Acceptor) Pro117 (Metal–Acceptor)	2.23 1.30 2.11 1.79 2.48 3.08	2	8	−11.90
5 *S. aureus*		-	-	Ile170 (Metal–Acceptor) Val49 (Metal–Acceptor) Leu197 (Metal–Acceptor) Gln105 (Metal–Acceptor) Thr200 (Metal–Acceptor) Thr227 (Metal–Acceptor) Arg239 (Metal–Acceptor) Leu198 (Metal–Acceptor) Asp45 (Metal–Acceptor) Ala237 (Metal–Acceptor) Val49 (Metal–Acceptor) Val196 (Metal–Acceptor)	3.30 2.77 1.30 2.75 2.86 3.32 2.12 1.65 3.36 1.52 3.39 2.91	0	12	−11.00
6 *S. haemolyticus*		Asp46 (H-Bond) Leu89 (H-Bond)	2.33 1.90	Gly29 (C-H bond) Asp90 (Metal–Acceptor) Asp48 (Metal–Acceptor) Asp46 (Metal–Acceptor) Trp26 (Metal–Acceptor) Asp153 (Metal–Acceptor) Asp46 (Metal–Acceptor) Ile91 (Metal–Acceptor) Leu89 (Metal–Acceptor)	2.22 2.20 2.01 1.98 1.56 2.91 3.01 1.54 3.26	2	11	−9.50

Ala: alanine, Arg: arginine, Asp: aspartic acid, Glu: glutamic acid, Gln: glutamine, Gly: glycine, Ile: isoleucine, Leu: leucine, Lys: lysine, Met: methionine, Phe: phenylalanine, Pro: proline, Ser: serine, Thr: threonine, Trp: tryptophan, Tyr: tyrosine, Val: Valine.
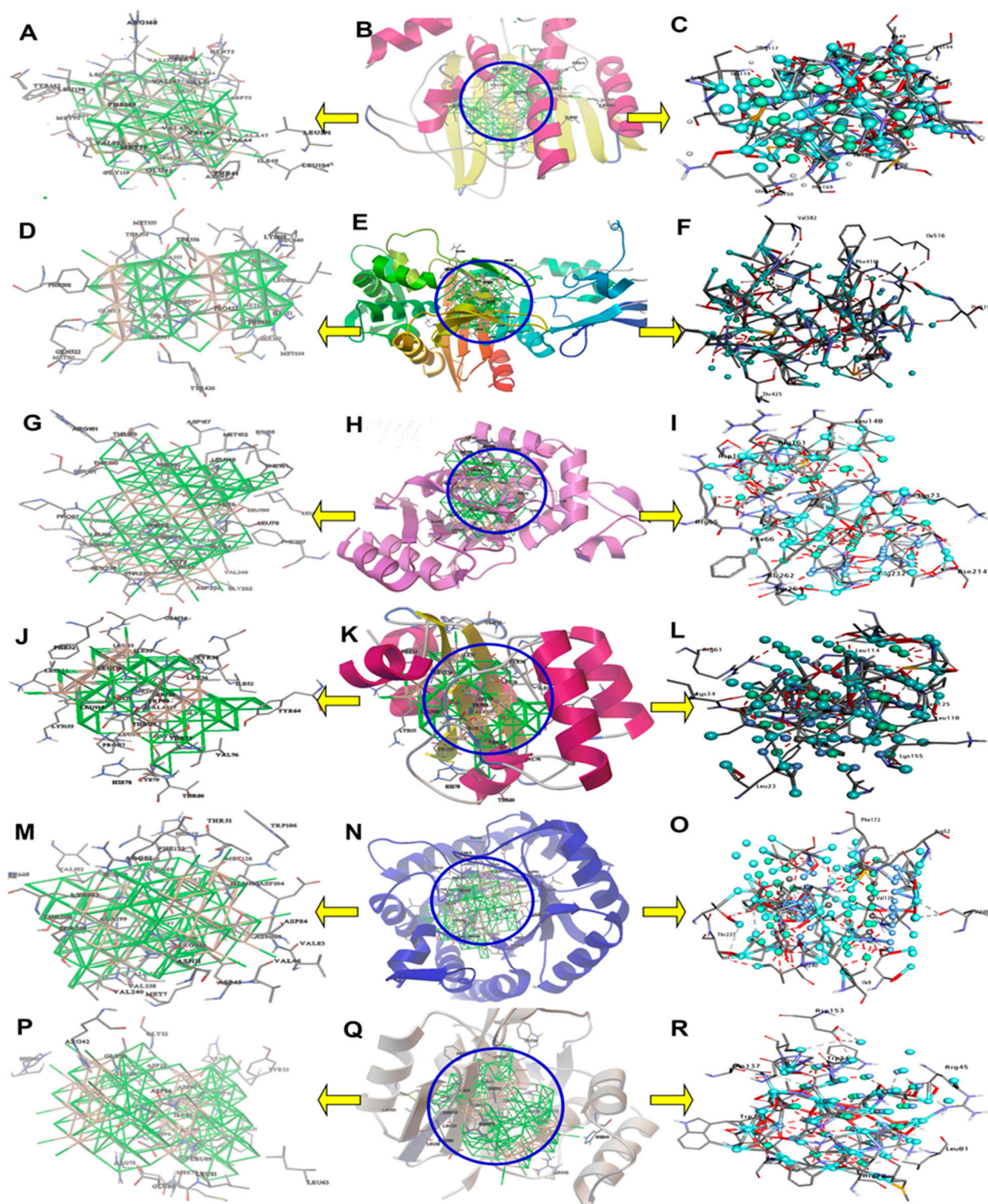
Figure 13. Three-dimensional complex of doped AgNP conformations at the binding pocket. The left side shows feature interactions between residues and doped AgNPs; the right side shows chemical structures of doped AgNPs and interacting amino acid residues according to their type: (**A–C**) DNA gyrase of *E.coli*, (**D–F**) penicillin-binding proteins of *E. faecalis*, (**G–I**) KPC-2 carbapenemase of *K. pneumoniae*, (**J–L**) LASR-binding domain of *P. aeruginosa*, (**M–O**) dihydropteroate synthase of *S. aureus* (PDB: ID 1AD4), and (**P–R**) lincosamide adenylyl transferase of *S. haemolyticus*.

The KPC-2 carbapenemase enzyme is a significant factor contributing to antibiotic resistance in K. pneumoniae. Classified under class A of beta-lactamases, KPC-2 plays a crucial role in this resistance mechanism. According to the docking results, the doped Ag-NPs exhibited affinity interactions measuring −10.20 kcal/mol. Interestingly, no hydrogen bonds were formed with the doped AgNPs. Instead, the interactions were characterized by nine metal–acceptor bonds involving Leu148, Met152, Tyr247, Thr235, Gly232, Arg161, Thr180, Asp157, and Phe66, showcasing hydrophobic connections with the doped AgNPs (Figure 13G–I).

The LasR-binding protein, produced by *P. aeruginosa*, contributes to the pathogenicity. The estimated binding energies revealed strong affinity interactions of −11.90 kcal/mol. Notably, the doped AgNPs formed two hydrogen bonds with Lys34 and Gly126. Furthermore, the hydrophobic interactions with the doped AgNPs involved six metal–acceptor bonds with Phe51, Gly38, Ser129, Lys34, Gly126, and Pro117 (Figure 13J–L). These findings are in line with the research conducted by El-Sayed et al. (2024), who utilized computational tools to elucidate how synthesized Cu-doped ZnO could potentially serve as inhibitors of the LasR-binding protein, shedding light on their inhibitory effects [73].

DHPS plays a crucial role in folate biosynthesis within *S. aureus*, acting as a key enzyme in nucleotide synthesis and essential cellular functions. Docking results revealed that doped AgNPs demonstrated an affinity of −11.00 kcal/mol. The doped AgNPs did not engage in hydrogen bonding. Instead, the interactions were characterized by twelve metal–acceptor bonds involving Ile170, Val49, Leu197, Gln105, Thr200, Thr227, Arg239, Leu198, Asp45, Ala237, Val49, and Val196, constituting the hydrophobic interactions with the doped AgNPs (Figure 13M–O).

Finally, the lincosamide adenylyl transferase enzyme, produced by *S. haemolyticus*, is responsible for conferring resistance to lincosamide antibiotics. The doped AgNPs exhibited an affinity of −9.50 kcal/mol. Notably, they formed two hydrogen bonds with Asp46 and Leu89. Also, the doped AgNPs established a carbon–hydrogen bond with Gly29 and five metal–acceptor bonds involving Asp90, Asp48, Asp46, Trp26, Asp153, Ile91, and Leu89, contributing to the interactions with the enzyme (Figure 13P–R).

4. Conclusions

Our study focused on synthesizing doped AgNPs with Gd, Cr, and Y using the PNLE. The XRD patterns revealed the crystallinity and purity of the NPs. The other characterization techniques showed the spherical shape of the NPs, with particle sizes ranging between 18 and 26 nm, with different functional groups. Surface plasmon resonance with an intense peak was observed at 283 nm and 414 nm by UV–vis spectrophotometric measurements with the optimized values. In addition, visible photoluminescence emission was observed within the 450–700 nm wavelength range, with peak emissions between 456 and 620 nm. For the magnetization properties, the NPs were ferromagnetic with saturation magnetization of 0.836 emu/g. Regarding the biological application, the doped AgNPs exerted significant antibacterial and antibiofilm activities, with better actions against Gram-positive bacteria in various concentrations. Furthermore, the doped AgNPs showed significant antioxidant activity against DPPH. The findings from the docking studies suggest that doped AgNPs can inhibit pivotal enzymes like DNA gyrase, penicillin-binding proteins, carbapenemase, LasR-binding proteins, and dihydropteroate synthase. Moreover, the antibacterial properties of these doped AgNPs are linked to their interference with critical bacterial processes. Finally, this study opens an avenue to use the doped AgNPs prepared from the PNLE in different medical domains, especially against urinary tract infections caused by uro-pathogenic bacteria.

References

1. Micoli, F.; Bagnoli, F.; Rappuoli, R.; Serruto, D. The role of vaccines in combatting antimicrobial resistance. *Nat. Rev. Microbiol.* **2021**, *19*, 287–302. [CrossRef] [PubMed]
2. Liguori, K.; Keenum, I.; Davis, B.C.; Calarco, J.; Milligan, E.; Harwood, V.J.; Pruden, A. Antimicrobial Resistance Monitoring of Water Environments: A Framework for Standardized Methods and Quality Control. *Environ. Sci. Technol.* **2022**, *56*, 9149–9160. [CrossRef] [PubMed]
3. Fernandes, M.; González-Ballesteros, N.; Da Costa, A.; Machado, R.; Gomes, A.C.; Rodríguez-Argüelles, M.C. Antimicrobial and anti-biofilm activity of silver nanoparticles biosynthesized with *Cystoseira algae* extracts. *JBIC J. Biol. Inorg. Chem.* **2023**, *28*, 439–450. [CrossRef] [PubMed]
4. Ndeh, D.; Rogowski, A.; Cartmell, A.; Luis, A.S.; Baslé, A.; Gray, J.; Venditto, I.; Briggs, J.; Zhang, X.; Labourel, A.; et al. Complex pectin metabolism by gut bacteria reveals novel catalytic functions. *Nature* **2017**, *544*, 65–70. [CrossRef] [PubMed]
5. Rajendran, R.; Mani, A. Photocatalytic, antibacterial and anticancer activity of silver-doped zinc oxide nanoparticles. *J. Saudi Chem. Soc.* **2020**, *24*, 1010–1024. [CrossRef]
6. Salem, S.S.; EL-Belely, E.F.; Niedbała, G.; Alnoman, M.M.; Hassan, S.E.-D.; Eid, A.M.; Shaheen, T.I.; Elkelish, A.; Fouda, A. Bactericidal and In-Vitro Cytotoxic Efficacy of Silver Nanoparticles (Ag-NPs) Fabricated by Endophytic Actinomycetes and Their Use as Coating for the Textile Fabrics. *Nanomaterials* **2020**, *10*, 2082. [CrossRef]
7. Shehabeldine, A.M.; Amin, B.H.; Hagras, F.A.; Ramadan, A.A.; Kamel, M.R.; Ahmed, M.A.; Atia, K.H.; Salem, S.S. Potential Antimicrobial and Antibiofilm Properties of Copper Oxide Nanoparticles: Time-Kill Kinetic Essay and Ultrastructure of Pathogenic Bacterial Cells. *Appl. Biochem. Biotechnol.* **2023**, *195*, 467–485. [CrossRef]
8. Roy, A.; Srinivas, V.; Ram, S.; Rao, T.V.C. The effect of silver coating on magnetic properties of oxygen-stabilized tetragonal Ni nanoparticles prepared by chemical reduction. *J. Phys. Condens. Matter* **2007**, *19*, 346220. [CrossRef]
9. Tariq, M.; Mohammad, K.N.; Ahmed, B.; Siddiqui, M.A.; Lee, J. Biological Synthesis of Silver Nanoparticles and Prospects in Plant Disease Management. *Molecules* **2022**, *27*, 4754. [CrossRef]
10. Akter, M.; Sikder, M.T.; Rahman, M.M.; Ullah, A.K.M.A.; Hossain, K.F.B.; Banik, S.; Hosokawa, T.; Saito, T.; Kurasaki, M. A systematic review on silver nanoparticles-induced cytotoxicity: Physicochemical properties and perspectives. *J. Adv. Res.* **2018**, *9*, 1–16. [CrossRef]
11. Singh, G.; Katoch, M. Antimicrobial activities and mechanism of action of *Cymbopogon khasianus* (Munro ex Hackel) Bor essential oil. *BMC Complement. Med. Ther.* **2020**, *20*, 331. [CrossRef] [PubMed]
12. Breznica, P.; Koliqi, R.; Daka, A. A review of the current understanding of nanoparticles protein corona composition. *Med. Pharm. Rep.* **2020**, *93*, 342–350. [CrossRef] [PubMed]
13. Kapoor, R.T.; Salvadori, M.R.; Rafatullah, M.; Siddiqui, M.R.; Khan, M.A.; Alshareef, S.A. Exploration of Microbial Factories for Synthesis of Nanoparticles—A Sustainable Approach for Bioremediation of Environmental Contaminants. *Front. Microbiol.* **2021**, *12*, 658294. [CrossRef] [PubMed]
14. Singh, P.; Pandit, S.; Jers, C.; Joshi, A.S.; Garnæs, J.; Mijakovic, I. Silver nanoparticles produced from *Cedecea* sp. exhibit antibiofilm activity and remarkable stability. *Sci. Rep.* **2021**, *11*, 12619. [CrossRef]
15. Singh, P.; Pandit, S.; Garnæs, J.; Tunjic, S.; Mokkapati, V.; Sultan, A.; Thygesen, A.; Mackevica, A.; Mateiu, R.V.; Daugaard, A.E.; et al. Green synthesis of gold and silver nanoparticles from *Cannabis sativa* (industrial hemp) and their capacity for biofilm inhibition. *Int. J. Nanomed.* **2018**, *13*, 3571–3591. [CrossRef]
16. Shenoy, R.U.K.; Rama, A.; Govindan, I.; Naha, A. The purview of doped nanoparticles: Insights into their biomedical applications. *OpenNano* **2022**, *8*, 100070. [CrossRef]
17. Darwich, N.A.; Mezher, M.; Abdallah, A.M.; El-Sayed, A.F.; El Hajj, R.; Hamdalla, T.A.; Khalil, M.I. Green Synthesis of Yttrium Derivatives Nanoparticles Using Pine Needle Leaf Extract: Characterization, Docking, Antibacterial, and Antioxidant Potencies. *Processes* **2024**, *12*, 1713. [CrossRef]
18. Blomqvist, L.; Nordberg, G.F.; Nurchi, V.M.; Aaseth, J.O. Gadolinium in Medical Imaging—Usefulness, Toxic Reactions and Possible Countermeasures—A Review. *Biomolecules* **2022**, *12*, 742. [CrossRef]

19. Khan, S.A.; Shahid, S.; Hanif, S.; Almoallim, H.S.; Alharbi, S.A.; Sellami, H. Green Synthesis of Chromium Oxide Nanoparticles for Antibacterial, Antioxidant Anticancer, and Biocompatibility Activities. *Int. J. Mol. Sci.* **2021**, *22*, 502. [CrossRef]

20. Gyawali, N.; Kandel, R.; Lee, I.; Shrestha, S.; Pandey, A.; Akter, J.; Ryang, J. Silver decoration of Cr_2O_3 nanoparticles: Facile preparation of Cr_2O_3 nanoparticles and $Ag–Cr_2O_3$ nanocomposites and characterization of their antibacterial activity and ability to photocatalytically degrade organic wastes under visible light. *J. Photochem. Photobiol. A Chem.* **2024**, *47*, 115251. [CrossRef]

21. Prabitha, V.G.; Sahadevan, J.; Madhavan, M.; Muthu, S.E.; Kim, I.; Sudheer, T.K.; Sivaprakash, P. Effect of Yttrium doping on antibacterial and antioxidant property of $LaTiO_3$. *Discov. Nano* **2023**, *18*, 155. [CrossRef] [PubMed]

22. Aashima; Pandey, S.K.; Singh, S.; Mehta, S.K. Biocompatible gadolinium oxide nanoparticles as efficient agent against pathogenic bacteria. *J. Colloid Interface Sci.* **2018**, *529*, 496–504. [CrossRef] [PubMed]

23. Mezher, M.; Hajj, R.E.; Khalil, M. Investigating the antimicrobial activity of essential oils against pathogens isolated from sewage sludge of southern Lebanese villages. *GERMS* **2022**, *12*, 488–506. [CrossRef]

24. Adnan, R.; Abdallah, A.M.; Mezher, M.; Noun, M.; Khalil, M.; Awad, R. Impact of Mg-doping on the structural, optical, and magnetic properties of CuO nanoparticles and their antibiofilm activity. *Phys. Scr.* **2023**, *98*, 055935. [CrossRef]

25. Adnan, R.M.; Mezher, M.; Abdallah, A.M.; Awad, R.; Khalil, M.I. Synthesis, Characterization, and Antibacterial Activity of Mg-Doped CuO Nanoparticles. *Molecules* **2022**, *28*, 103. [CrossRef] [PubMed]

26. Rabaa, M.; Mezher, M.; Aridi, A.; Naoufal, D.; Khalil, M.I.; Awad, R.; Abdeen, W. Influence of Lanthanum Doping on the Photocatalytic and Antibacterial Capacities of $Mg_{0.33}Ni_{0.33}Co_{0.33}Fe_2O_4$ Nanoparticles. *Catalysts* **2023**, *13*, 693. [CrossRef]

27. Rabaa, M.; Mezher, M.; Aridi, A.; Naoufal, D.; Khalil, M.; Awad, R. Improved Photocatalytic and Antibacterial Activity of $Mg_{0.33}Ni_{0.33}Co_{0.33}Gd_xFe_{2-x}O_4$ Nanoparticles Synthesized via the Co-precipitation Method. *ChemistrySelect* **2023**, *8*, e202301951. [CrossRef]

28. Baliyan, S.; Mukherjee, R.; Priyadarshini, A.; Vibhuti, A.; Gupta, A.; Pandey, R.P.; Chang, C.-M. Determination of Antioxidants by DPPH Radical Scavenging Activity and Quantitative Phytochemical Analysis of Ficus religiosa. *Molecules* **2022**, *27*, 1326. [CrossRef]

29. Shabnam, N.; Sharmila, P.; Kim, H.; Pardha-Saradhi, P. Light Mediated Generation of Silver Nanoparticles by Spinach Thylakoids/Chloroplasts. *PLoS ONE* **2016**, *11*, e0167937. [CrossRef]

30. Sharifi-Rad, M.; Pohl, P.; Epifano, F.; Álvarez-Suarez, J.M. Green Synthesis of Silver Nanoparticles Using Astragalus tribuloides Delile. Root Extract: Characterization, Antioxidant, Antibacterial, and Anti-Inflammatory Activities. *Nanomaterials* **2020**, *10*, 2383. [CrossRef]

31. Jing, Y.; Lei, Q.; Xia, C.; Guan, Y.; Yang, Y.; He, J.; Yang, Y.; Zhang, Y.; Yan, M. Synthesis of Ag and AgCl co-doped ZIF-8 hybrid photocatalysts with enhanced photocatalytic activity through a synergistic effect. *RSC Adv.* **2020**, *10*, 698–704. [CrossRef] [PubMed]

32. López-Miranda, J.L.; Mares-Briones, F.; Silva, R.; Esparza, R.; Estevez, M. Green synthesis and characterization of metallic nanoparticles with environmental applications. *MRS Adv.* **2023**, *8*, 1172–1176. [CrossRef]

33. Raj, S.; Trivedi, R.; Soni, V. Biogenic Synthesis of Silver Nanoparticles, Characterization and Their Applications—A Review. *Surfaces* **2021**, *5*, 67–90. [CrossRef]

34. Ahmad, F.; Ashraf, N.; Ashraf, T.; Zhou, R.-B.; Yin, D.-C. Biological synthesis of metallic nanoparticles (MNPs) by plants and microbes: Their cellular uptake, biocompatibility, and biomedical applications. *Appl. Microbiol. Biotechnol.* **2019**, *103*, 2913–2935. [CrossRef] [PubMed]

35. Annamalai, N.; Thavasi, R.; Vijayalakshmi, S.; Balasubramanian, T. A novel thermostable and halostable carboxymethylcellulase from marine bacterium Bacillus licheniformisAU01. *World J. Microbiol. Biotechnol.* **2011**, *27*, 2111–2115. [CrossRef]

36. Anandalakshmi, K.; Venugobal, J.; Ramasamy, V. Characterization of silver nanoparticles by green synthesis method using Pedalium murex leaf extract and their antibacterial activity. *Appl. Nanosci.* **2016**, *6*, 399–408. [CrossRef]

37. Al-Bataineh, Q.M.; Ababneh, R.; Bahti, A.; Bani-Salameh, A.A.; Tavares, C.J.; Telfah, A. Effect of hydrogen-related shallow donor on the physical and chemical properties of Ag-doped ZnO nanostructures. *J. Mater. Sci. Mater. Electron.* **2022**, *33*, 17434–17445. [CrossRef]

38. Kanwal, Z.; Raza, M.A.; Riaz, S.; Manzoor, S.; Tayyeb, A.; Sajid, I.; Naseem, S. Synthesis and characterization of silver nanoparticle-decorated cobalt nanocomposites (Co@AgNPs) and their density-dependent antibacterial activity. *R. Soc. Open Sci.* **2019**, *6*, 182135. [CrossRef]

39. Labulo, A.H.; David, O.A.; Terna, A.D. Green synthesis and characterization of silver nanoparticles using *Morinda lucida* leaf extract and evaluation of its antioxidant and antimicrobial activity. *Chem. Pap.* **2022**, *76*, 7313–7325. [CrossRef]

40. Asif, M.; Yasmin, R.; Asif, R.; Ambreen, A.; Mustafa, M.; Umbreen, S. Green Synthesis of Silver Nanoparticles (AgNPs), Structural Characterization, and their Antibacterial Potential. *Dose-Response* **2022**, *20*, 155932582210887. [CrossRef]

41. Arya, S.K.; Dey, A.; Bhansali, S. Polyaniline protected gold nanoparticles based mediator and label free electrochemical cortisol biosensor. *Biosens. Bioelectron.* **2011**, *28*, 166–173. [CrossRef] [PubMed]

42. Lin, Z.Y.; Xiao, J.; Yan, J.H.; Liu, P.; Li, L.H.; Yang, G.W. Ag/AgCl plasmonic cubes with ultrahigh activity as advanced visible-light photocatalysts for photodegrading dyes. *J. Mater. Chem. A* **2015**, *3*, 7649–7658. [CrossRef]

43. Zhang, Y.; Alagic, Z.; Tani, E.; Skorpil, M.; Tsagkozis, P.; Haglund, F. Clear-cell chondrosarcomas: Fine-needle aspiration cytology, radiological findings, and patient demographics of a rare entity. *Diagn. Cytopathol.* **2021**, *49*, 46–53. [CrossRef] [PubMed]

44. Duc Chinh, V.; Speranza, G.; Migliaresi, C.; Van Chuc, N.; Minh Tan, V.; Phuong, N.-T. Synthesis of Gold Nanoparticles Decorated with Multiwalled Carbon Nanotubes (Au-MWCNTs) via Cysteaminium Chloride Functionalization. *Sci. Rep.* **2019**, *9*, 5667. [CrossRef]

45. Song, J.-B.; Kim, J.-T.; Oh, S.-G.; Yun, J.-Y. Contamination Particles and Plasma Etching Behavior of Atmospheric Plasma Sprayed Y_2O_3 and YF_3 Coatings under NF_3 Plasma. *Coatings* **2019**, *9*, 102. [CrossRef]

46. Elemike, E.E.; Onwudiwe, D.C.; Ekennia, A.C.; Jordaan, A. Synthesis and characterisation of silver nanoparticles using leaf extract of *Artemisia afra* and their in vitro antimicrobial and antioxidant activities. *IET Nanobiotechnol.* **2018**, *12*, 722–726. [CrossRef]

47. Zhang, X.; Yang, C.; Zhou, J.; Huo, M. Somatostatin Receptor-Mediated Tumor-Targeting Nanocarriers Based on Octreotide-PEG Conjugated Nanographene Oxide for Combined Chemo and Photothermal Therapy. *Small* **2016**, *12*, 3578–3590. [CrossRef]

48. Chang, M.; Tie, S. Fabrication of novel luminor Y_2O_3: Eu^{3+}@SiO_2@YVO_4:Eu^{3+} with core/shell heteronanostructure. *Nanotechnology* **2008**, *19*, 075711. [CrossRef]

49. Suriyakala, G.; Sathiyaraj, S.; Devanesan, S.; AlSalhi, M.S.; Rajasekar, A.; Maruthamuthu, M.K.; Babujanarthanam, R. Phytosynthesis of silver nanoparticles from *Jatropha integerrima* Jacq. flower extract and their possible applications as antibacterial and antioxidant agent. *Saudi J. Biol. Sci.* **2022**, *29*, 680–688. [CrossRef]

50. Hachem, Z.; Kashmar, R.; Abdallah, A.M.; Awad, R.; Khalil, M.I. Characterization, antioxidant, antibacterial, and antibiofilm properties of biosynthesized Ag/AgCl nanoparticles using *Origanum ehrenbergii* Boiss. *Results Mater.* **2024**, *21*, 100550. [CrossRef]

51. Harshapriya, P.; Basandrai, D.; Kaur, P. Structural and optical properties of Yttrium-Silver doped ZnO nanoparticle. *Mater. Today Proc.* **2023**, *4*, S2214785323003267. [CrossRef]

52. Juluri, M.; Mohammed, R.A.; Mohan, S.; Golla, N.; Krishna, S.B.N.; Battini, K. Green synthesis, characterization and biological activities of silver nanoparticles synthesized from *Neolamarkia cadamba*. *ADMET DMPK* **2023**, *11*, 573–585. [CrossRef]

53. Coates, J. Interpretation of Infrared Spectra, A Practical Approach. In *Encyclopedia of Analytical Chemistry*; Meyers, R.A., Ed.; Wiley: Hoboken, NJ, USA, 2000. [CrossRef]

54. Jagathy, K.; Malathi, S. Characterization and Green Biosynthesis of Silver Nanoparticles using Raphanus sativus and its Antibacterial Activity against Urinary Tract Infection Causing *E. coli. Int. J. Curr. Res. Rev.* **2021**, *13*, 40–45. [CrossRef]

55. Thirunavoukkarasu, M.; Balaji, U.; Behera, S.; Panda, P.K.; Mishra, B.K. Biosynthesis of silver nanoparticle from leaf extract of *Desmodium gangeticum* (L.) DC. and its biomedical potential. *Spectrochim. Acta. A. Mol. Biomol. Spectrosc.* **2013**, *116*, 424–427. [CrossRef] [PubMed]

56. Aghazadeh, M.; Ghaemi, M.; Nozad Golikand, A.; Yousefi, T.; Jangju, E. Yttrium Oxide Nanoparticles Prepared by Heat Treatment of Cathodically Grown Yttrium Hydroxide. *ISRN Ceram.* **2011**, *2011*, 542104. [CrossRef]

57. Jain, S.; Mehata, M.S. Medicinal Plant Leaf Extract and Pure Flavonoid Mediated Green Synthesis of Silver Nanoparticles and their Enhanced Antibacterial Property. *Sci. Rep.* **2017**, *7*, 15867. [CrossRef]

58. Saranya, D.; Sekar, J. GC-MS and FT-IR Analyses of Ethylacetate Leaf extract of *Abutilon indicum* (L.) Sweet. *Int. J. Adv. Res. Biol. Sci.* **2016**, *3*, 193–197.

59. Benammar, I.; Salhi, R.; Deschanvres, J.-L.; Maalej, R. The effect of rare earth element (Er, Yb) doping and heat treatment on suspension stability of Y_2O_3 nanoparticles elaborated by sol-gel method. *J. Mater. Res. Technol.* **2020**, *9*, 12634–12642. [CrossRef]

60. Ali, I.A.M.; Ahmed, A.B.; Al-Ahmed, H.I. Green synthesis and characterization of silver nanoparticles for reducing the damage to sperm parameters in diabetic compared to metformin. *Sci. Rep.* **2023**, *13*, 2256. [CrossRef]

61. Yaqoob, A.A.; Ahmad, H.; Parveen, T.; Ahmad, A.; Oves, M.; Ismail, I.M.I.; Qari, H.A.; Umar, K.; Mohamad Ibrahim, M.N. Recent Advances in Metal Decorated Nanomaterials and Their Various Biological Applications: A Review. *Front. Chem.* **2020**, *8*, 341. [CrossRef]

62. Francis, S.; Joseph, S.; Koshy, E.P.; Mathew, B. Microwave assisted green synthesis of silver nanoparticles using leaf extract of *Elephantopus scaber* and its environmental and biological applications. *Artif. Cells Nanomed. Biotechnol.* **2018**, *46*, 795–804. [CrossRef] [PubMed]

63. Gong, R.; Chen, G. Preparation and application of functionalized nano drug carriers. *Saudi Pharm. J.* **2016**, *24*, 254–257. [CrossRef] [PubMed]

64. Benedec, D.; Oniga, I.; Cuibus, F.; Sevastre, B.; Stiufiuc, G.; Duma, M.; Hanganu, D.; Iacovita, C.; Stiufiuc, R.; Lucaciu, C.M. Origanum vulgare mediated green synthesis of biocompatible gold nanoparticles simultaneously possessing plasmonic, antioxidant and antimicrobial properties. *Int. J. Nanomed.* **2018**, *13*, 1041–1058. [CrossRef] [PubMed]

65. Radičić, R.; Maletić, D.; Blažeka, D.; Car, J.; Krstulović, N. Synthesis of Silver, Gold, and Platinum Doped Zinc Oxide Nanoparticles by Pulsed Laser Ablation in Water. *Nanomaterials* **2022**, *12*, 3484. [CrossRef] [PubMed]

66. Yamamoto, Y.; Miura, T.; Suzuki, M.; Kawamura, N.; Miyagawa, H.; Nakamura, T.; Kobayashi, K.; Teranishi, T.; Hori, H. Direct Observation of Ferromagnetic Spin Polarization in Gold Nanoparticles. *Phys. Rev. Lett.* **2004**, *93*, 116801. [CrossRef]

67. Amiar Rodin, N.L.; Sahar, M.R.; Mohd-Noor, F. Magnetic analysis of cobalt oxide nanoparticles comprised boro-tellurite glass with erbium lanthanide. *J. Magn. Magn. Mater.* **2020**, *496*, 165931. [CrossRef]

68. Kowalik, P.; Mikulski, J.; Borodziuk, A.; Duda, M.; Kamińska, I.; Zajdel, K.; Rybusinski, J.; Szczytko, J.; Wojciechowski, T.; Sobczak, K.; et al. Yttrium-Doped Iron Oxide Nanoparticles for Magnetic Hyperthermia Applications. *J. Phys. Chem. C* **2020**, *124*, 6871–6883. [CrossRef]

69. Ullah, A.K.M.A.; Kabir, M.F.; Akter, M.; Tamanna, A.N.; Hossain, A.; Tareq, A.R.M.; Khan, M.N.I.; Kibria, A.K.M.F.; Kurasaki, M.; Rahman, M.M. Green synthesis of bio-molecule encapsulated magnetic silver nanoparticles and their antibacterial activity. *RSC Adv.* **2018**, *8*, 37176–37183. [CrossRef]

70. Dagher, L.A.; Hassan, J.; Kharroubi, S.; Jaafar, H.; Kassem, I.I. Nationwide Assessment of Water Quality in Rivers across Lebanon by Quantifying Fecal Indicators Densities and Profiling Antibiotic Resistance of *Escherichia coli*. *Antibiotics* **2021**, *10*, 883. [CrossRef]

71. Huq, M.A.; Khan, A.A.; Alshehri, J.M.; Rahman, M.S.; Balusamy, S.R.; Akter, S. Bacterial mediated green synthesis of silver nanoparticles and their antibacterial and antifungal activities against drug-resistant pathogens. *R. Soc. Open Sci.* **2023**, *10*, 230796. [CrossRef]

72. Sudarsan, S.; Kumar Shankar, M.; Kumar Belagal Motatis, A.; Shankar, S.; Krishnappa, D.; Mohan, C.D.; Rangappa, K.S.; Gupta, V.K.; Siddaiah, C.N. Green Synthesis of Silver Nanoparticles by *Cytobacillus firmus* Isolated from the Stem Bark of *Terminalia arjuna* and Their Antimicrobial Activity. *Biomolecules* **2021**, *11*, 259. [CrossRef] [PubMed]

73. Sayed, F.A.-Z.; Eissa, N.G.; Shen, Y.; Hunstad, D.A.; Wooley, K.L.; Elsabahy, M. Morphologic design of nanostructures for enhanced antimicrobial activity. *J. Nanobiotechnol.* **2022**, *20*, 536. [CrossRef] [PubMed]

74. Arya, A.; Tyagi, P.K.; Bhatnagar, S.; Bachheti, R.K.; Bachheti, A.; Ghorbanpour, M. Biosynthesis and assessment of antibacterial and antioxidant activities of silver nanoparticles utilizing *Cassia occidentalis* L. seed. *Sci. Rep.* **2024**, *14*, 7243. [CrossRef] [PubMed]

75. Yılmaz, Ç.; Özcengiz, G. Antibiotics: Pharmacokinetics, toxicity, resistance and multidrug efflux pumps. *Biochem. Pharmacol.* **2017**, *133*, 43–62. [CrossRef] [PubMed]

76. CLSI. *M100 Performance Standards for Antimicrobial Susceptibility Testing*, 33rd ed.; M100ED33; Clinical and Laboratory Standards Institute: Wayne, PA, USA, 2023.

77. Nazzaro, F.; Fratianni, F.; De Martino, L.; Coppola, R.; De Feo, V. Effect of Essential Oils on Pathogenic Bacteria. *Pharmaceuticals* **2013**, *6*, 1451–1474. [CrossRef]

78. Iseppi, R.; Tardugno, R.; Brighenti, V.; Benvenuti, S.; Sabia, C.; Pellati, F.; Messi, P. Phytochemical Composition and In Vitro Antimicrobial Activity of *Essential oils* from the Lamiaceae Family against *Streptococcus agalactiae* and *Candida albicans* Biofilms. *Antibiotics* **2020**, *9*, 592. [CrossRef]

79. Khalid, A.; Ahmad, P.; Alharthi, A.I.; Muhammad, S.; Khandaker, M.U.; Rehman, M.; Faruque, M.R.I.; Din, I.U.; Alotaibi, M.A.; Alzimami, K.; et al. Structural, Optical, and Antibacterial Efficacy of Pure and Zinc-Doped Copper Oxide Against Pathogenic Bacteria. *Nanomaterials* **2021**, *11*, 451. [CrossRef]

80. Famuyide, I.M.; Aro, A.O.; Fasina, F.O.; Eloff, J.N.; McGaw, L.J. Antibacterial and antibiofilm activity of acetone leaf extracts of nine under-investigated south African Eugenia and Syzygium (Myrtaceae) species and their selectivity indices. *BMC Complement. Altern. Med.* **2019**, *19*, 141. [CrossRef]

81. Aires, A.; Barreto, A.S.; Semedo-Lemsaddek, T. Antimicrobial Effects of Essential Oils on Oral Microbiota Biofilms: The Toothbrush In Vitro Model. *Antibiotics* **2020**, *10*, 21. [CrossRef]

82. Bedlovičová, Z.; Strapáč, I.; Baláž, M.; Salayová, A. A Brief Overview on Antioxidant Activity Determination of Silver Nanoparticles. *Molecules* **2020**, *25*, 3191. [CrossRef]

83. Siddique, M.A.B.; Imran, M.; Haider, A.; Shahzadi, A.; Ul-Hamid, A.; Nabgan, W.; Batool, M.; Khan, K.; Ikram, M.; Somaily, H.H.; et al. Enhancing catalytic and antibacterial activity with size-controlled yttrium and graphene quantum dots doped MgO nanostructures: A molecular docking analysis. *Mater. Today Sustain.* **2024**, *25*, 100690. [CrossRef]

84. Ikram, M.; Shujah, T.; Shahzadi, A.; Haider, A.; Rafique, A.; Ul-Hamid, A.; Nabgan, W.; Haider, S.K.; Alshahrani, T.; Algaradah, M.M.; et al. Multiple phases of yttrium-doped molybdenum trioxide nanorods as efficient dye degrader and bactericidal agents with molecular docking analysis. *Chemosphere* **2023**, *340*, 139855. [CrossRef] [PubMed]